

GIANT PLANET MIGRATION THROUGH THE ACTION OF DISK TORQUES AND PLANET-PLANET SCATTERING

Althea V. Moorhead¹ and Fred C. Adams^{1,2}

¹*Michigan Center for Theoretical Physics
Physics Department, University of Michigan, Ann Arbor, MI 48109*

²*Astronomy Department, University of Michigan, Ann Arbor, MI 48109*

ABSTRACT

This paper presents a parametric study of giant planet migration through the combined action of disk torques and planet-planet scattering. The torques exerted on planets during Type II migration in circumstellar disks readily decrease the semi-major axes a , whereas scattering between planets increases the orbital eccentricities ϵ . This paper presents a parametric exploration of the possible parameter space for this migration scenario using two (initial) planetary mass distributions and a range of values for the time scale of eccentricity damping (due to the disk). For each class of systems, many realizations of the simulations are performed in order to determine the distributions of the resulting orbital elements of the surviving planets; this paper presents the results of ~ 8500 numerical experiments. Our goal is to study the physics of this particular migration mechanism and to test it against observations of extrasolar planets. The action of disk torques and planet-planet scattering results in a distribution of final orbital elements that fills the $a - \epsilon$ plane, in rough agreement with the orbital elements of observed extrasolar planets. In addition to specifying the orbital elements, we characterize this migration mechanism by finding the percentages of ejected and accreted planets, the number of collisions, the dependence of outcomes on planetary masses, the time spent in 2:1 and 3:1 resonances, and the effects of the planetary IMF. We also determine the distribution of inclination angles of surviving planets and the distribution of ejection speeds for exiled planets.

Keywords: Extrasolar planets – planetary dynamics – planetary formation

1. Introduction

With over one hundred extrasolar planets discovered thus far, the past decade has witnessed a revolution in our understanding of planetary systems. The initial discoveries (Mayor and Queloz

1995; Marcy and Butler 1996) showed that the orbital elements of the extrasolar planets are significantly different from those of the planets in our solar system. Some fraction of the giant planets are found in short period orbits with $P_{\text{orb}} \approx 4$ days (semi-major axes $a \approx 0.05$ AU), while others display longer period orbits of high eccentricity $0 \leq \epsilon \leq 0.9$ (where the high end of this range remains somewhat uncertain). Subsequent discoveries have shown that such planetary systems are relatively common and have a rich variety of architectures (e.g., Marcy and Butler 1998, 2000; Hatzes et al. 2000; Perryman 2000). In particular, the observed planets populate a large portion of the $a - \epsilon$ plane. An important astronomical challenge is to provide a theoretical explanation for the observed distributions of orbital elements. A related challenge is to understand the physical mechanism through which planets migrate inward from their birth sites.

This paper presents a theoretical study of giant planet migration through the combined action of disk torques and scattering by other planets in the system. We consider planets of Jovian mass (in order of magnitude) so that the planets clear gaps in the disk and thus experience Type II migration. During the epoch of planet formation and migration, both gaseous circumstellar disks and multiple planets are expected to be present. Sufficiently massive disks are effective at exerting torques on planets and moving them inward, thereby changing their semi-major axes a . Scattering interactions between planets are effective at increasing the orbital eccentricities ϵ (this point was emphasized in Adams and Laughlin 2003; hereafter AL2003). This paper presents a statistically comprehensive study of this migration mechanism and demonstrates that the interplay between these two effects leads to a rich variety of possible outcomes. Because these systems cover a wide range of parameter space and tend to be chaotic, this process results in a broad distribution for the orbital elements of the final systems. This model – Type II migration driven by interactions with a circumstellar disk and by dynamical scattering from other planets – naturally produces the entire possible range of semi-major axis a and eccentricity ϵ .

This research builds on an extensive body of previous work. Migration was anticipated long before extrasolar planets were detected (e.g., Goldreich and Tremaine 1980; Lin and Papaloizou 1993) and a host of different migration mechanisms have been developed (see the review of Ward and Hahn 2000). Type I migration occurs when a planet (or forming planet) is too small to clear a gap in the disk and remains embedded within the fluid (Ward 1997); the planet drives wakes into the background gas of the disk and these wakes, in turn, exert torques on the planet and push it inward. In this study, we assume that the planets are already formed and are large enough to clear gaps in the disk, so that the starting point of these calculations takes place after Type I migration has run its course (although it remains possible for these early stages to provide an alternate explanation of the observed orbital elements). This paper considers a parametric treatment that corresponds to Type II migration, wherein the planet clears a gap in the gaseous disk. Many studies of Type II migration have been carried out to explain the newly discovered extrasolar planets in short period orbits (e.g., Lin et al. 1996; Trilling et al. 1998; Nelson et al. 2000; Bryden et al. 2000; Bate et al. 2003), although such models generally do not readily explain the large eccentricities observed in many planetary orbits. For completeness we note that additional models of runaway migration

have been proposed as a way to explain “hot Jupiters” (sometimes called Type III migration – see Masset and Snellgrove 2001; Masset and Papaloizou 2003), although they are not considered here.

Another way to achieve shorter periods is through gravitational scattering interactions with a disk of planetesimals (Murray et al. 1998), although this mechanism requires a great deal of mass in solid materials inside the orbit of the giant planet (see also the Appendix to AL2003). A complementary collection of papers has studied migration through planet-planet scattering alone, starting with two planets (Rasio and Ford 1996; Weidenschilling and Marzari 1996; Katz 1997) and continuing with more complicated configurations (Ford et al. 2001; Marzari and Weidenschilling 2002; Papaloizou and Terquem 2002; AL2003). These studies indicate that planet scattering is highly effective at producing large orbital eccentricities but does not readily move planets inward to small semi-major axes. Specifically, the ratio of the initial to final semi-major axes, a_0/a_f , is typically only 3 – 5, and a larger ratio would require a great deal of additional mass in scattering bodies (more than is thought to be available in such disks).

In light of the aforementioned research, one economical way to explain both the observed (small) semi-major axes and the observed (large) eccentricities is through a combined model with disk torques and multiple planets (Lin and Ida 1997; Kley 2000; AL2003; Thommes and Lissauer 2003; Kley et al. 2004). Many of the previous studies focus on explaining particular observed two-planet systems like GJ876 (e.g., Snellgrove et al. 2001; Lee and Peale 2002; Murray et al. 2002) and 47 UMa (Laughlin et al. 2002). This paper adopts a more general treatment.

This present work has two modest goals: The first objective is to explore the physics of this migration mechanism by extending previous calculations to encompass a wider range of parameter space. This work is a straightforward generalization of AL2003, but extends that paper in several ways: [1] In addition to the random mass distribution of AL2003, this paper considers a a log-random initial mass function for the planets. [2] This paper explores a much wider range of time scales for eccentricity damping due to the disk. [3] This paper includes starting configurations that lead to the planets being initially caught in both the 2:1 and 3:1 mean motion resonances, and we track how long the planets stay near resonance. [4] The distributions of ejection velocities for escaping planets are determined. [5] In order to isolate the effects of the input parameters on the final results, this paper presents the orbital elements both immediately after planets are lost and after corrections for additional evolution are taken into account. [6] This work includes a tenfold increase in the number of numerical simulations and hence in coverage of parameter space (for a total of ~ 8500 trials).

The second goal of this paper is to determine if this migration mechanism can account for the orbital elements of the observed extrasolar planets. Since the observed orbital elements of these planetary systems explore (nearly) the full range of possible semi-major axis and eccentricity, filling the $a - \epsilon$ plane is a necessary, but not sufficient, condition on a complete theory of planet migration. The mechanism explored here can be made consistent with the observed orbital element distributions, but such a comparison is preliminary and caution should be taken.

2. Methods and Initial Conditions

This section outlines our basic migration model which combines the dynamical interactions between two planets with inward forcing driven by tidal interactions with a background nebular disk, i.e., Type II migration (see also Kley 2000; Murray et al. 2002; Papaloizou 2003; Kley et al. 2004). Our goal here is to build on previous studies by producing a statistical generalization of the generic migration problem with two planets and an exterior disk – a situation that we expect is common during the planet formation process.

The numerical experiments are set up for two planets with the following orbital properties: Two planets are assumed to form within a circumstellar disk with initial orbits that are widely spaced. The central star is assumed to be of solar-type with mass $M_* = 1.0 M_\odot$. For the sake of definiteness, the inner planet is always started with orbital period $P_{in} = 1900$ days, which corresponds to a semi-major axis $a_{in} \approx 3$ AU. This radial location lies just outside the snowline for most models of circumstellar disks and thus provides a fiducial starting point where the innermost giant planets are likely to form. For most of the simulations, the second (outer) planet is placed on an orbit with the larger period $P_{out} = \pi 2^{1/4} P_{in} \approx (3.736 \dots) P_{in}$. With this starting state, the planets are not initially in resonance but will first encounter the 3:1 resonance as the outer planet migrates inward. As the system evolves, the two orbits become closer together. With these starting states, the planets are sometimes caught in the 3:1 resonance, but often pass through and approach the 2:1 resonance. In an alternate set of starting states, the outer planet is given an initial orbital period $P_{out} = e P_{in} \approx (2.718 \dots) P_{in}$ so that the planets start inside the 3:1 resonance but outside the 2:1 resonance. In either case, the two planets are often caught in mean motion resonances for some portion of their evolution (for a more detailed description, see Lee and Peale 2002). In practice, the initial period ratio is likely to have a distribution, but this paper focuses on these two specific choices. The initial eccentricities of both planets are drawn from a uniform random distribution in the range $0 < \epsilon < 0.05$. The planets are also started with a small, but nonzero inclination angle in the range $i \leq 0.03$ (in radians). Planetary systems started in exactly the same orbital plane tend to stay co-planar, whereas small departures such as these allow the planets to explore the full three dimensions of space.

In this study we use two different distributions for the starting planetary masses. We denote the planetary mass distribution as the IMF (the initial mass function) where it should be understood that we mean planet masses (not stellar masses). The first IMF is a uniform random distribution in which the planet masses m_P are drawn independently from the range $0 < m_P < 5m_J$, where m_J is the mass of Jupiter. In the second mass distribution, denoted as the log-random IMF, the logarithm of the planet mass $\log_{10}[m_P/m_J]$ is drawn independently from the interval $-1 \leq \log_{10}[m_P/m_J] \leq 1$. The random mass distribution provides a good starting point to study the physics of these systems – it provides a good sampling of the possible masses and mass ratios that two planet systems can have. On the other hand, the observed distribution of planet masses is much closer to a log-random distribution, so this latter distribution provides a better model for comparison with observations. One result of this work is a determination of how this migration mechanism changes the planetary

IMF, and it is useful to study this evolution from the two different starting distributions.

The numerical integrations are carried out using a Bulirsch-Stoer scheme (Press et al. 1986). The equations of motion are those of the usual three body problem (two planets and the star) with the following additional forcing terms: The circumstellar disk exerts torques on the planets which lead to both orbital decay (Type II migration) and damping of eccentricity. The star exerts tidal forces on the planets which leads to additional energy dissipation and partial circularization of the orbits. Finally, the leading order curvature of space-time (due to general relativity) is included to properly account for the periastron advance of the orbits.

The outer planet in the system is tidally influenced by a background circumstellar disk. Since the planets are (roughly) of Jovian mass, they clear gaps in the disk and experience Type II migration. Instead of modeling the interaction between the outer planet and disk in detail, we adopt a parametric treatment that introduces a frictional damping term into the dynamics. This damping force has the simple form $\mathbf{f} = -\mathbf{v}\tau_{\text{damp}}^{-1}$ and is applied to the outer planet at each time step, as a torque $\mathbf{r} \times \mathbf{f}$, so the outer planet is gradually driven inward. The assumed damping force is proportional to the velocity and defines a disk accretion time scale τ_{damp} . We assume here that the disk inside the orbit of the outer planet is sufficiently cleared out so that the inner planet does not usually experience a Type II torque. Over most of its evolution, the inner planet has a sufficiently small eccentricity so that it lies well inside the (assumed) gap edge and receives negligible torque from the disk (which lies outside the outer planet). When the inner planet attains a high eccentricity, however, it can be found at a radius comparable to that of the outer planet and can thus experience some torque. This (relatively minor) effect is included by giving the inner planet a torque that is reduced from that of the outer planet by a factor $(r_{\text{in}}/r_{\text{out}})^6$.

In this set of simulations, we set the accretion time scale to be $\tau_{\text{damp}} = 0.3$ Myr, consistent with recent estimates of this quantity. We can compare this time scale to several reference points: [1] For example, Nelson et al. (2000) advocate migration time scales of 10^4 orbits for Jovian mass planets. [2] If disk accretion is driven by viscous diffusion and can be described by an α prescription, then the disk accretion time scale $\tau_{\text{disk}} = \varpi^2/\nu$, where the viscosity $\nu = (2/3)\alpha v_T^2 \Omega^{-1}$ (Shu 1992). The disk scale height H can be written in the form $H = v_T/\Omega$, where v_T is the sound speed, and the accretion time becomes $\tau_{\text{disk}} = 1.5(\varpi/H)^2 \Omega^{-1} \alpha^{-1}$. If we evaluate the disk scale height H and rotation rate Ω for a temperature of $T = 70$ K at $\varpi = 7$ AU (where the outer planet forms and begins its migration), the adopted disk accretion time scale $\tau_{\text{damp}} = 0.3$ Myr corresponds to $\alpha = 7 \times 10^{-4}$. This value falls comfortably within the expected range $10^{-4} \leq \alpha \leq 10^{-2}$ (see Shu 1992). [3] As another point of comparison, three-dimensional simulations of Jovian planets in circumstellar disks (Kley, D’Angelo, and Henning 2001) find similar migration time scales, about 0.1 Myr, which agree with two-dimensional simulations done previously (Kley 1999). In these numerical studies, the disks have slightly larger $\alpha = 4 \times 10^{-3}$ (hence the slightly shorter time scale), scale height $H/r = 0.05$, and disk mass $M_d = 3.5 \times 10^{-3} M_\odot$ within the annulus $2 \text{ AU} \leq r \leq 13 \text{ AU}$. Note that the disk mass must be larger than the planet masses in order to drive Type II migration. Notice also that the migration time scale is assumed to be independent of the orbital eccentricity, although

more complicated behavior is possible.

These simulations include an additional forcing term that damps the eccentricity of the outer planetary orbit (as suggested by numerical simulations of these systems). In other words, the same angular momentum exchange between the disk and the planet that leads to orbital migration can also modify the eccentricity of the orbit. Unfortunately, previous work on this issue presents rather divergent points of view. Most numerical studies indicate that the action of disk torques leads to damping of eccentricity, and these results are often supported by analytic calculations (e.g., Snellgrove et al. 2001; Schäfer et al. 2004). On the other hand, competing analytic calculations indicate that eccentricity can be excited through the action of disk torques and this mechanism has been proposed as an explanation for the observed high eccentricities in the extrasolar planetary orbits (e.g., Ogilvie and Lubow 2003; Goldreich and Sari 2003; Papaloizou et al. 2001). One reason for this ambiguity is that the interaction between the disk and the planet can be broken down into the action of resonances in the disk, where the non-coorbital corotation resonances act to damp the eccentricity of the planetary orbits while the non-coorbital Lindblad resonances act to pump it up. The net effect depends on a close competition between the damping terms and the excitation terms. In rough terms, the conditions that result in eccentricity damping are those that lead to relatively narrow gaps, which in turn correspond to large disk viscosity ($\alpha \sim 10^{-3}$) and modest sized planet masses ($m_P \sim m_J$) as assumed here. The disk surface density and scale height also play a role (Bryden et al. 2000). If the gap is not completely clear, then the corotation resonance locations within the gap will contain gas that can interact with the planet and help enforce eccentricity damping (S. Lubow, private communication; this issue is quite complicated and warrants further discussion — see Ogilvie and Lubow 2003, Goldreich and Sari 2003). In contrast, wide and clear gaps, which result from smaller viscosity and/or larger planet masses ($m_P \approx 10 - 20m_J$), can lead to eccentricity excitation (Snellgrove et al. 2001; Papaloizou et al. 2001).

In light of these ambiguities, we incorporate the effects of eccentricity damping in a parametric manner. For completeness, we note that the damping force described above (that which enforces inward migration) also tends to damp the eccentricity, although this effect is much smaller than the explicit eccentricity damping terms included here. Specifically, the orbital eccentricity of the outer planet is damped on a time scale τ_{ed} , which is considered as a free parameter in this treatment. The eccentricity damping is enforced by converting the cartesian variables to orbital elements (a, ϵ, i) , applying the damping term, and then converting back. The inclination angle is not explicitly damped, although the outer planet experiences a small damping effect due to the form of the migration force. In this work, we explore a range of damping times scales $0.1 \text{ Myr} \leq \tau_{\text{ed}} \leq \infty$, where the $\tau_{\text{ed}} \rightarrow \infty$ limit corresponds to no eccentricity damping. We have also run test cases in which τ_{ed} varies with orbital eccentricity, so that more eccentric orbits are damped to a greater extent, although the results are not markedly different. Our numerical exploration of parameter space suggests that the most relevant variable is the ratio of eccentricity damping time to disk accretion time, where this ratio falls in the range $1/3 \leq \tau_{\text{ed}}/\tau_{\text{damp}} \leq \infty$ for the simulations presented here. For comparison, the full range of positive values for this ratio considered in the literature is

approximately $0.01 \leq \tau_{\text{ed}}/\tau_{\text{damp}} \leq \infty$ (with an additional range of negative values corresponding to eccentricity excitation). This paper considers the more limited range because the behavior outside our range is known: For small values of $\tau_{\text{ed}}/\tau_{\text{damp}}$, eccentricity damping is highly efficient, few planets are ejected, and large eccentricities are not produced (e.g., Lee and Peale 2002; Thommes and Lissauer 2003). For negative values of $\tau_{\text{ed}}/\tau_{\text{damp}}$, eccentricity is excited. We find that even with no eccentricity damping, this model tends to overproduce eccentricity relative to the currently observed sample of extrasolar planets; eccentricity excitation could lead to even larger discrepancies. Note that one advantage of this parametric treatment is that thousands of simulations can be performed and the full distributions of final orbital elements can be determined.

The numerical code includes relativistic corrections to the force equations (e.g., Weinberg 1972). This force contribution drives the periastron of both planetary orbits to precess (in the forward direction). Because the effect is greater close to the star, the inner planet experiences more precession, and the net effect is to move the two planets away from resonance. If the planets migrate sufficiently close to the central star, this differential precession effect can keep the planets out of a perfect resonance. Since resonant conditions lead to greater excitation of orbital eccentricity, which in turns drives the system toward instability, this relativistic precession acts to make planetary systems more stable. In these simulations, however, the planets rarely migrate close enough to the star to make this effect important, but it is included for completeness.

The simulations also include energy lost due to tidal interactions between the planets and their central stars. In these simulations, the planets spend most of their time relatively far from the star where tidal interactions are negligible. As a result, we adopt a simplified treatment of this effect. Specifically, the force exerted on the planet due to tidal interactions is written in the approximate form

$$\mathbf{F} = -\frac{Gm_P R_*^5}{Cj r^{11}} [r^2 \mathbf{v} - (\mathbf{r} \cdot \mathbf{v}) \mathbf{r}] \frac{0.6r_p^3}{1 + (r_p/R_*)^3}, \quad (1)$$

where R_* is the radius of the star, r_p is the distance of closest approach for a parabolic orbit with angular momentum j , and $C = 2\sqrt{\pi}/3$ is a dimensionless constant of order unity (for further discussion, see Papaloizou and Terquem 2001; Press and Teukolsky 1977). This formula implicitly assumes that the time between encounters is long compared to the time for tidal interaction itself and that most of the forcing occurs near the point of closest approach. This approximation is valid when the close encounters occur due to planetary orbits with high eccentricities, which is generally the case for planets in these simulations. Note that for longer term evolution of close planetary orbits, such as circularization over Gyr time scales, an alternate approximation for the tidal forces is necessary (see Section 4.2).

The simulations allow for collisions to take place between the planets, and between the planets and the star. The effective radius for planetary collisions is taken to be $R_P = 2R_J$, with cross section $\sigma_P = 4\pi R_J^2$, which implicitly assumes that the planets have not fully contracted. In order to model accretion events, we assume that when a planet wanders within a distance $d = 2 \times 10^{11}$ cm of the central star, accretion takes place. This distance corresponds to $d \sim 3R_\odot$, which is a typical

radius for solar type stars during the early part of their pre-main-sequence phase of evolution.

For a given set of starting conditions (described above), each numerical experiment is integrated forward in time and the system follows the same basic evolutionary trend (see Fig. 1 and Section 3): The planets are started with a sufficient separation so that they have weak initial interactions and are far from resonance. As the outer planet migrates inward through the action of disk torques, the planets often enter into a mean motion resonance, usually the 3:1 or 2:1 resonance because of the starting conditions. The tendency to enter 3:1 versus 2:1 resonances varies with the planetary IMF, with a linear IMF producing more planets in 3:1 resonances and a log IMF producing more 2:1 systems. In addition, the 2:1 resonances last longer, implying that they are more stable. The two planets then migrate inwards together, staying relatively close to resonance, but displaying ever larger librations as the orbital eccentricities of both planets increase (on average). The eccentricities increase until the system (often) becomes unstable, and a wide range of final system properties can result. In practice, we continue the simulations until one of the following stopping criteria is met: A planet is ejected, the planets collide with each other, a planet is accreted by the central star, or a maximum integration time limit is reached (set here to be 1.0 Myr). This latter time scale represents the time over which the disk contains enough mass to drive inward migration of planets; the disk could retain enough gas to exhibit observational signatures over a longer time.

After a planet is lost (through ejection, accretion, or collision), the numerical integration is stopped and the orbital elements of the surviving planet are recorded. In general, however, the orbital elements of the surviving planet can continue to evolve after a planet is lost as long as the disk is still present. In order to separate the effects of the combined migration mechanism (i.e., Type II migration with planet scattering) from the additional evolution, we first present the results with no additional evolution in the following section. In order to compare with the observed orbital elements of extrasolar planets, we consider possible algorithms for this additional evolution in Section 4.

3. Results from the Numerical Simulations

This paper presents the results of an ensemble of ~ 8500 simulations that follow the early evolution of two-planet solar systems subjected to disk torques using the methodology described above. The simulations use two different planetary IMFs and, for each IMF, four choices of the eccentricity damping time scale τ_{ed} . For each set of these input parameters, we completed approximately 800 – 1000 solar system simulations. We then determined the resulting distributions of semi-major axis a , eccentricity ϵ , inclination angle i , and surviving planetary mass m_P . These results can be used to quantify the outcome of this migration mechanism (see below) and can be compared to observed distributions of orbital elements in extrasolar planetary systems (Section 4).

3.1. Evolution of Orbital Elements

To illustrate the general behavioral trend of these systems, we follow the evolution of orbital elements for a collection of representative simulations. The result of one such run is shown in Fig. 1. The first panel shows how the semi-major axis of each planet decreases smoothly with time; this basic trends holds for essentially all cases. In the second panel of Fig. 1, we plot the period ratio of the two planets, and find that it quickly approaches and remains near 3. This result indicates that the two planets may be in a 3:1 mean motion resonance (see Section 3.3 for further discussion). This behavior occurs during the early evolution for the majority of cases, although in some cases the outer planet passes through the 3:1 period ratio (and hence the 3:1 resonance) and the period ratio remains near ~ 2 for most of the evolution. In other systems, the period ratio remains near 3 for the early evolution, and then the planets move through the 3:1 resonance, become closer, and reside near the 2:1 resonance for the latter part of the simulation. A more detailed accounting of how long various systems spend near the 3:1 and 2:1 resonances is given below (Section 3.3).

The behavior of eccentricity and inclination angle is more complex. We find that orbital eccentricity increases steeply in the beginning, and then undergoes oscillations about an average value that increases at a slower rate. The eccentricity exhibits varying behaviors over different spans of time and varies substantially from case to case. In the more stable systems, the eccentricity values level off and experience variations about the mean. In unstable cases, the eccentricities are driven to ever larger values until a planet is either ejected or accreted onto the central star. The inclination angle experiences a similar evolutionary trend.

This complex behavior of the orbital element leads to a distribution of final values. To illustrate this sensitive dependence on the initial conditions, we have run a set of numerical experiments with equal mass planets, an eccentricity damping time scale $\tau_{\text{ed}} = 1$ Myr, and starting configurations with the outer planet outside the 3:1 resonance. The starting values of the angular orbital elements are chosen to vary randomly from case to case. The results are shown in Fig. 2 for the case of two $m_P = 1.0m_J$ planets (top two panels) and two $m_P = 5.0m_J$ planets (bottom two panels). For the case of smaller planets ($1 m_J$), both planets survive the entire 1.0 Myr time span of the simulations, but they attain a wide distribution of final orbital elements. For the case of larger planets ($5m_J$), one of the planets is always ejected, whereas the remaining planet attains a distribution of orbital elements as shown. Fig. 2 shows that effectively equivalent starting conditions lead to a well-defined distribution of outcomes. In other words, for this class of simulations, the outcomes must be described in terms of the distributions of a or ϵ , rather than as particular values of a or ϵ .

3.2. End State Probabilities

The simulations end in a variety of different states, including ejection, accretion, collision, or the survival of both planets past the fiducial time span of one million years. The frequencies of each fate are listed in Table 1 for varying eccentricity damping time scales and for both planetary

IMFs. The number of ejected planets depends sensitively on the IMF: Only one third of the planets were ejected for a logarithmic IMF, whereas more than half were ejected for a linear IMF. This behavior is expected because the linear IMF provides more massive planets, which in turn produce a disturbing function of greater magnitude and lead to more frequent ejection. We also find that the outer planet is more than 3–4 times as likely to be the ejected planet, and the inner planet is almost always the accreted planet. The incidence of each end state exhibits no clear trend with respect to eccentricity damping time scale (for a given planetary IMF). For the case in which the planets are started just outside the 2:1 resonance (inside the 3:1 resonance), the end state probabilities are similar, but show a slight preference for accretion relative to ejection (see Table 1).

Averaged over all outcomes, the mean time of the simulations (which end when a planet is lost) is about 0.5 Myr; this time scale is roughly comparable to the viscous damping time of $\tau_{\text{damp}} = 0.3$ Myr. Accretion events take the longest, with an average time of 0.55 Myr; ejection events have a mean time of 0.22 Myr; collisions take place the fastest with a mean time of only 0.10 Myr.

The end states depend on the planet masses in a systematic way, as shown in Figs. 3 and 4, which show the various possible end states as a function of the masses. For systems in which the outer planet is substantially more massive than the inner one, $m_{\text{out}} \gg m_{\text{in}}$, the inner planet is nearly always driven to high eccentricities and accreted onto the central star (as shown by the blue diamonds in Figs. 3 and 4). In the opposite limit where $m_{\text{out}} \ll m_{\text{in}}$, the outer planet tends to be ejected (as shown by the green squares in the figures). When both planets are massive, corresponding to the upper right portion of the mass plane, either planet can be readily ejected. When both planets have relatively low masses, corresponding to the lower left portion of the mass plane, both planets tend to survive (shown by the cross symbols in the figures).

Tables 2 – 4 present the distributions of mass m_P , semi-major axis a , and eccentricity ϵ at the end of the simulations. Each entry lists the mean value of the distribution as well as its width (variance). Table 2 presents the planetary masses for all cases, including planets that are lost (ejected planets and accreted planets). The following tables list the parameters that characterize the distributions of semi-major axis (Table 3) and orbital eccentricity (Table 4) for the planets that remain at the end of the simulations. For accretion or ejection events (of either planet), the distributions of semi-major axis, eccentricity, and mass are roughly similar for a given planetary IMF and varying τ_{ed} (although variations do exist, especially at the extremes of our chosen range of τ_{ed}). The collisions result in significantly different orbital properties (not listed in the Tables), with smaller eccentricity ϵ and larger mass m_P . The other general trend that emerges from this suite of simulations is that the systems that remain stable over the entire 1 Myr integration time are those with the smallest planets, with a mean mass of only $0.79 m_J$ (for the log-random IMF, averaged over the four values of τ_{ed}) compared to a mean mass $m_P = 2.8 m_J$ for the whole ensemble.

For the log-random IMF, which is closest to producing the observed mass distribution, roughly one third of the systems retain both planets at the end of the 1 Myr integration time (see Table 1). For comparison, about 10 – 20 percent of the observed extrasolar planetary systems show multiple

planets (to date – see www.exoplanets.org). However, the theoretical systems that retain multiple planets tend to have planetary masses that are smaller than average (Table 2) and such low mass planets may have escaped detection. In addition, as many as half of the systems observed with one planet may contain additional bodies (Fischer et al. 2001). More data is necessary to determine whether or not this issue is problematic for the theory.

3.3. Behavior of Resonance Angles

As shown above, the period ratio of the two planets quickly and smoothly approaches an integer value, often 3, and thus approaches a mean motion resonance. As one benchmark, 70% of the systems studied here spend at least 10,000 years near the 3:1 resonance. This result is supported by the behavior of the 3:1 resonance angles over time. To illustrate this behavior we focus on the three angles

$$\phi_1 = 3\lambda_2 - \lambda_1 - 2\varpi_1, \quad \phi_2 = 3\lambda_2 - \lambda_1 - \varpi_2 - \varpi_1, \quad \phi_3 = 3\lambda_2 - \lambda_1 - 2\varpi_2, \quad (2)$$

where the λ_j are the mean longitudes and the ϖ_j are the longitudes of pericenter (Murray and Dermott 2001). Note that a complete description of the 3:1 resonance requires three additional angles, although their behavior is similar to those considered here. For the representative case of two planets of one Jupiter mass each, Fig. 5 shows how the system passes through different versions of the 3:1 resonances. For example, between 50 and 200 thousand years, the first three angles librate about values that are 120 degrees apart. Then, between 0.25 and 1 Myr, the first and third angles librate about an angular value that is 180 degrees different from the second.

A wide range of behavior is displayed in the time evolution of the resonance angles, although the overall defining trend can be described as follows (see also Beaugé et al. 2003; Ferraz-Mello et al. 2003; Lee 2004): The planets tend to approach a mean motion resonance, but generally exhibit large librations about a perfect resonant condition. Two effects contribute to this behavior. The circumstellar disk exerts a torque on the outer planet and acts to move the planet inward and away from resonance; although the inner planet experiences a greatly reduced torque, it is not enough to keep up, and the two planets must continually readjust their orbital elements to maintain a resonant condition. In addition, the planets are massive enough and sufficiently close together so that they tend to excite the orbital eccentricities; this continual pumping up of the eccentricities can eventually act to make the system unstable. Notice that when the planets have low masses, they tend to stay in resonance longer. Indeed, at the end of the simulations, the subset of solar systems that retain both planets over the entire 1 Myr time period have a much lower average mass (see Table 2, Figs. 3 and 4, and the previous subsection).

Although most of these two-planet systems spend some of their evolutionary time in states with period ratio near 3:1, a substantial fraction of the systems pass through the 3:1 resonance and approach a 2:1 period ratio. One should keep in mind that a rational period ratio is a necessary, but not sufficient, condition for being in a mean motion resonance. For the ensemble of simulations

studied here, we have kept track of the time for which the planets display period ratios near 3:1 and near 2:1 (specifically, period ratios within 3 ± 0.15 and 2 ± 0.15 , respectively). The results are compiled in Table 5. The first four columns give the percentage of the time spent in (near) each resonance, where the first value in each table entry corresponds to the 2:1 resonance and the second value to the 3:1 resonance. Here, for the first four columns of results, the percentage is calculated by integrating up the total time that any planet in the given ensemble spends near the resonance and then dividing by the total time that the ensemble of planets resides in the simulations. Notice that this figure of merit is different from that obtained by finding the percentage of time that each individual planet spends near resonance, and then averaging that fraction over the planets; this latter quantity is given in the last column in Table 5 for the total samples (including all outcomes) for each planetary IMF.

For the linear IMF, Table 5 indicates that planets spend about 70 percent of their evolutionary time with period ratios of 3:1 and only about 20 percent of their time with ratios near 2:1. The planets that survive the longest (from the simulations that reach the stopping time of 1 Myr without losing a planet) tend to reach the 2:1 resonance (see below). As a result, the resonance fractions obtained by time averaging over the whole ensemble of planets (the percentages given in column 4 in Table 5) are more weighted toward the 2:1 resonance than the fractions obtained by finding the individual resonance time fractions and then averaging (the alternate percentages given in column 5). Similarly, for the log-random IMF, the systems spend an average of 53 percent of their time with 2:1 period ratios and 38 percent of their time with 3:1 period ratios (averaged over the four values of τ_{ed}). The main difference between the two IMF choices is that the linear IMF has larger planets and mass ratios closer to unity; our numerical results indicate that this combination is more conducive to keeping the planets locked in the 3:1 resonant condition. For those systems that stay near a period ratio of 3:1 for more than 80 percent of their evolutionary time, the distribution of mass ratios $m_{\text{out}}/m_{\text{in}}$ is sharply peaked near unity, with a long tail to larger values. As a result, equal mass planets tend to stay near resonance longer. Systems with with the inner planet more massive than the outer planet tend to move away from resonance, often by ejecting the smaller planet, whereas systems with more massive outer planets often drive the smaller inner planet into the star.

Another related result concerns the systems that survive for the entire 1 Myr time span without ejecting a planet. As mentioned above, the planets in these systems have relatively lower masses (Table 2). For the log-random IMF, 69 percent of the surviving systems are found with period ratios near 2:1, 28 percent of the systems show period ratios near 3:1, and the remaining 3 percent are “far” from resonance. Thus, surviving systems tend to be those that pass through the 3:1 resonance and become locked into the 2:1 resonance. As expected, the surviving systems show a mass distribution that is weighted toward lower masses compared with the original log-random distribution (which is roughly consistent with the mass distribution of observed planets). The distribution of mass ratios $m_{\text{out}}/m_{\text{in}}$ is slanted toward values less than unity so that surviving systems tend to have the outer planet less massive than the inner planet. For the linear IMF, the

results are somewhat different, where 67 percent of the surviving systems have period ratios near 3:1 and the remaining 33 percent have 2:1 period ratios (see also Figs. 3 and 4).

3.4. Distributions of Orbital Elements

For each class of starting configuration, the simulations result in a distribution of final system properties. The starting states can be characterized by the planetary IMF, the eccentricity damping time scale τ_{ed} , and the initial period of the outer planet P_{out} (although most of our simulations use $P_{\text{out}} \approx 3.736P_{\text{in}}$). Each triple (IMF, τ_{ed} , P_{out}) thus leads to distributions of final orbital elements, as reported in Tables 2 – 4. For each end state of the simulations (ejection, accretion, etc.), these tables characterize the distributions of mass, eccentricity, and semi-major axes, by specifying their mean values and widths. One must keep in mind the probabilistic nature of this type of problem. The simulations act as a mapping from an initial space to a final one,

$$(\text{IMF}, \tau_{\text{ed}}, P_{\text{out}}) \rightarrow \{f_{\text{out}}, f_a(a), f_\epsilon(\epsilon), f_i(i), f_m(m_P), \dots\}, \quad (3)$$

where the entries on the left hand side are numbers (single values) and the entries f_j on the right hand side are distributions of values (e.g., f_{out} represents the fractional occurrence of each outcome, $f_a(a)$ is the distribution of semi-major axes, etc.).

The resulting distributions of orbital elements, and planet masses are plotted in Figs. 6 and 7. For comparison, these figures include the distributions of planet properties from the observed sample (see Section 4). The lower right panel of each figure shows the mass distribution of the planets that survive to the end of the simulations. The observed distribution of planets provides us with $m_P \sin i_{\text{obs}}$ (rather than m_P); to account for this ambiguity, we have used the quantity $2m_P \sin i_{\text{obs}}$ as a working mass estimate for specifying the “observed” mass distribution (notice also that the observational viewing angle is different from the usual definition of inclination angle as an orbital element so that $\sin i_{\text{obs}} \neq \sin i$). In spite of the tendency for smaller planets to be ejected, the linear IMF tends to roughly preserve its shape during the course of evolution (see Fig. 6). However, in comparison, the mass distribution of observed extrasolar planets has fewer high mass planets and more low mass planets and is thus closer to the log-random distribution (which we adopted as our second working IMF – see Fig. 7). Even with the ejection of the smaller planets, the log-random IMF model yields a final mass distribution that is close to the observed distribution. Some discrepancy occurs in the high mass tail, however, because our log-random distribution has an upper bound at $m_P = 10 m_J$. Our model also provides a small surplus of planets in the low mass tail, relative to the observed mass distribution, although this disagreement may be the result of less frequent detection of the smallest planets.

The different sets of simulations (two planetary IMFs and four values of the eccentricity damping time scale) tend to result in relatively flat distributions of the semi-major axis (see the upper left panels of Figs. 6 and 7). For the case of no eccentricity damping and a log-random IMF, however, the semi-major axis distribution of the surviving planets displays a broad peak near 1 AU.

As the eccentricity damping is increased (more damping with a shorter time scale τ_{ed}), this peak becomes even broader (flattens out) and moves toward lower values of a . Because Type II migration torques are effective at moving planets inward, and because of the random element introduced into the migration process (due to different starting angles and varying effective integration times), the resulting values of semi-major axis fill the entire range covered by current observations.

The distributions of eccentricities are shown in the upper right panels in Figs. 6 and 7. As expected, the distribution of eccentricity shifts toward lower values as the level of eccentricity damping is increased (i.e., as τ_{ed} decreases). The general trend is for the simulations to excite the orbital eccentricities to higher levels (averaged over the distribution) than those found in the observational sample. The exception to this rule occurs for the shortest eccentricity damping time scale $\tau_{\text{ed}} = 0.1$ Myr for the log-random planetary IMF: In this class of systems, the resulting distribution of eccentricity is shifted to lower values than the observed planetary orbits. Taken at face value (ignoring the possibility of selection effects in the observational sample), this set of results argues that, within the context of this migration scenario, the eccentricity damping time scale cannot be smaller than about $\tau_{\text{ed}} = 0.1$ Myr (otherwise, resulting eccentricities would be too low) or larger than about $\tau_{\text{ed}} = 1.0$ Myr (otherwise, ϵ values would be too large). We will return to this issue below.

The distributions of inclination angle are shown as the lower left panels in Figs. 6 and 7. The resulting distributions of the inclination angle appear to be largely independent of the eccentricity damping time scale τ_{ed} for both choices of planetary IMF. The distribution shows a well-defined peak near $i \approx 6$ degrees for the random IMF and a broader peak near $i = 3-5$ degrees for the log-random IMF. Although modest, these angles are significantly larger than the starting inclination angles ($|i| \leq 0.03 \approx 1.7$ degrees). For the shortest eccentricity damping time scale and the log-random IMF (which has the greatest number of small planets), however, the distribution of inclination angle is shifted somewhat toward lower values.

As a general rule, increases of the inclination angle are correlated with increases of eccentricity (consistent with the earlier studies of AL2003; Thommes and Lissauer 2003). For this ensemble of simulations, we find that the inclination angle and the eccentricity have a linear correlation coefficient in the range $r(N) \approx 0.33 - 0.66$ for simulations that end in either ejection or accretion. Table 6 shows these results for the eight classes of simulations conducted in this study; also shown (in parentheses) are the numbers of simulations in the sample used to compute each correlation coefficient. For the large sample size ($N \sim 100 - 300$), these values of $r(N)$ are generally considered significant (Press et al. 1986), but the correlation is not exact. Notice that our simple treatment does not include the possible damping of inclination angle by the circumstellar disk (e.g., Lubow and Ogilvie 2001). Such damping would move the distributions of i to smaller values, but the correlations between eccentricity excitation and inclination angle excitation would remain.

3.5. Distribution of Ejection Speeds

A substantial fraction of the planetary systems eject a planet and these planets can, in principle, be observed as free floating bodies. Table 1 indicates that approximately one-third of the systems will eject planets for the log-random planetary IMF, and over half of the systems with a linear IMF will eject planets. These planets have roughly Jovian mass (Table 2) and thus do not represent a significant mass contribution to the galaxy – in other words, the number of ejected planets is not large enough to be problematic. However, recent observations have found some evidence for freely floating planets (e.g., Zapatero Osorio et al. 2000) and these predicted planets must be consistent with the observations.

The planets are ejected with a well-defined distribution of speeds, as shown in Fig. 8. For all cases considered here, the distribution displays a well-defined peak near $v_{\text{ej}} = 5$ km/s and most of the distribution falls between 0.5 and 20 km/s. For comparison, the planets are ejected from orbits with semi-major axes near 3 – 7 AU, where the orbit speeds are about $11 - 17 \approx 14$ km/s. The kinetic energy carried away by the ejected planets is thus a small fraction \mathcal{F}_E of the total. A rough estimate of this fraction is given by

$$\mathcal{F}_E \approx \frac{v_{\text{ej}}^2/2}{|E|} = \frac{av_{\text{ej}}^2}{GM_*} \approx (5/14)^2 \approx 0.13, \quad (4)$$

where v_{ej} is the ejection speed and a is the semi-major axis from which ejection occurs. This finding vindicates the assumption that ejected planets tend to leave on (nearly) zero energy orbits (AL2003; Marzari and Weidenschilling 2002).

We can understand the general form of the distribution of ejection speeds with the following heuristic argument: Ejections occur through close encounters between the planets. Let b denote the impact parameter of these interactions, so that the ejection speed can be written

$$\frac{1}{2}v_{\text{ej}}^2 = \alpha \frac{G\langle m \rangle}{b} - \frac{GM_*}{2a}, \quad (5)$$

where a is the semi-major axis of the ejected planet (before the interaction), $\langle m \rangle$ is an average mass of the remaining planet, and α is a dimensionless factor of order unity (which depends on the geometry of the interaction). If we define a velocity scale $v_0^2 \equiv GM_*/a$ and a length scale $r_0 \equiv 2\alpha(\langle m \rangle/M_*)a$, the ejection speed can be written in the form

$$u = \left[\frac{1}{\xi} - 1 \right]^{1/2}, \quad (6)$$

where $u \equiv v_{\text{ej}}/v_0$ and $\xi \equiv b/r_0$. If we assume that the impact parameter is distributed according to $dP \propto bdb$ (the target area is circular), the probability distribution for the ejection speed takes the form

$$\frac{dP}{du} = \frac{4u}{(1+u^2)^3}. \quad (7)$$

As written, this probability distribution is normalized to unity over the full range of dimensionless ejection speeds $0 \leq u \leq \infty$. In practice, the impact parameter has a minimum value given by

the radius of the (ejector) planet, $b_{\min} = r_P$, and this value implies a corresponding cutoff in the ejection speed $v_{\max} \approx v_0 \sqrt{r_0/r_P}$. However, the distribution falls rapidly at high speeds so that the value of this cutoff is relatively unimportant. Equation (7) has the same form as the distributions of ejection speeds found in the simulations (as shown in Fig. 8). The model distribution has been normalized to agree with the simulations (note that the fraction of systems that experience ejection must be determined numerically). The distributions agree if the velocity scale is taken to be $v_0 \approx 11$ km/s, which implies that ejections (mostly) occur near the beginning of the evolution (the outer planets, which are more often ejected, start near 7 AU where $(GM_*/a) \approx 11$ km/s). Finally, we note that the simple formula derived above assumes a single value for the velocity scale. Since the planets can migrate inwards to different semi-major axes before ejection, the true distribution will have a range of v_0 values; although this range is relatively narrow in the present application, this effect tends to broaden the distribution of ejection speeds relative to equation (7).

Under a reasonable set of assumptions, we can estimate the expected population of free floating planets within a typical birth aggregate. The velocity dispersion for a young star forming group/cluster is about 1 km/s (Lada and Lada 2003; Porras et al. 2003). Given the distribution of ejection speeds (Fig. 8), the majority of ejected planets are predicted to be unbound to their birth clusters. As a first approximation, suppose that every solar system produces migrating planets and that one third of them eject planets (Table 1). Of the ejected planets, about one tenth remain bound to the group/cluster with ejection speeds $v_{\text{ej}} < 1$ km/s. For every 30 stars in the cluster, it will thus contain one freely floating planet that is gravitationally bound. The unbound planets have ejection speeds of ~ 5 km/s. For an average cluster size of $R \sim 1$ pc, the ejected planets would remain within their birth clusters for ~ 0.2 Myr. If the young group/cluster remains intact for 10 Myr, then 1/50th of the unbound planets will reside within the group/cluster at any given time, and the cluster will contain one unbound planet for every 150 stars. Given a fiducial group/cluster size of $N_* \approx 300$ stars (Lada and Lada 2003; Porras et al. 2003), stellar birth aggregates will have ~ 10 freely floating planets at low speeds ($v_{\text{ej}} \leq 1$ km/s) and ~ 2 freely floating planets at higher speeds ($v_{\text{ej}} \sim 5$ km/s) at any given time ($t \leq 10$ Myr).

4. Comparison with Observed Extrasolar Planets

In order for a migration mechanism to be considered fully successful, it must produce distributions of orbital elements that are consistent with those of observed extrasolar planets. Given that the observed distributions are incomplete and contain biases, however, and that additional orbital evolution must take place between the end of our simulations and the $\sim 1 - 6$ Gyr ages of the observed systems, this type of comparison remains preliminary. In this section, we briefly discuss the limitations of the data set and outline how the distributions of orbital elements can evolve after the end of our simulations. We then show that this migration mechanism meets the necessary (but not sufficient) condition of being able to fill the $a - \epsilon$ plane in a manner that is roughly consistent with presently available data.

4.1. Observed Sample of Extrasolar Planets

The observed sample of extrasolar planets used in this paper is taken from the California and Carnegie Planet Search Website.¹ In order to compare theoretical results with this data set, some of its properties must be taken into account. All planet searches using radial velocity surveys are subject to selection effects. Since the surveys are subject to a minimum (detectable) velocity amplitude, planetary companions that induce reflex velocities that are too small cannot be measured. This effect limits the sensitivity of the surveys to low mass planets. In addition, planets with long periods (large semi-major axes a) cannot be adequately detected because of the limited time baseline of the surveys. This latter effect thus leads to a loss of sensitivity at large a . As a benchmark, Jupiter produces a 12.5 m/s velocity variation on the Sun with a period of 12 years. The detection of a Solar System analog requires approximately $k \approx 3$ m/s precision maintained over a decade window of observing (Paul Butler, private communication). Since this level of precision (Bernstein et al. 2003) and this time baseline are the best that are currently available, the mass and semi-major axis of Jupiter represent a rough upper limit on detectability. As a general rule, the completeness of the data set must decline with increasing semi-major axis and decreasing planet mass. The detection limit can be written in terms of the reflex velocity k_{re} , defined by

$$k_{\text{re}} \equiv \frac{m_P \sin i_{\text{obs}}}{M_*^{2/3} (1 - \epsilon^2)^{1/2}} \left(\frac{2\pi G}{P} \right)^{1/3}, \quad (8)$$

which is valid in the limit $m_P \ll M_*$. We can scale this formula to the limit quoted above, i.e., that the detection of Jupiter itself is near the present day observational threshold. The portion of the $a - \epsilon$ plane that is accessible to observations is (conservatively) delimited by the curve $a(1 - \epsilon^2) \leq 5\mu^2$, where a is in AU and $\mu = m_P \sin i_{\text{obs}}$ is in Jupiter masses. The radial velocity surveys have 7 year time spans (for the latter, more complete samples) which implies a limit of about $a \leq 3.5$ AU for completeness in semi-major axis. For this value of a , the corresponding mass limit is thus $\mu \geq 0.84 (1 - \epsilon^2)^{1/2}$. As a result, for the moderate eccentricities observed, $\langle \epsilon \rangle \approx 0.3$, the sample is expected to be nearly complete out to $a = 3.5$ AU for $m_P \sin i_{\text{obs}} \geq 0.8m_J$, and nearly complete at $a = 1$ AU for $m_P \sin i_{\text{obs}} \geq 0.43m_J$. At the low end of our planetary IMF, $m_P \sim 0.1m_J$, the observed sample is expected to be missing planets.

For planets detected with incomplete data sampling, the derived orbital eccentricities are subject to uncertainties. If a planet has extremely low eccentricity, then noise in the radial velocity data stream can mimic the signature of small eccentricities. On the other hand, extrasolar planets with the highest eccentricities, say $\epsilon > 0.8$, may be subject to an additional bias that makes them hard to detect using available strategies, which are sparsely sampled in time (due to limited telescope resources). Planets on high eccentricity orbits spend most of their time out near apastron, where they produce little radial velocity variation. Unless the system is observed when the planet is near periastron, it is difficult to determine the true eccentricity. Even when such a planet is detected,

¹<http://exoplanets.org/science.html>

the analysis can underestimate the eccentricity until enough data has been obtained to provide full orbital phase coverage (e.g., see Naef et al. 2001 and the case of HD 80606). However, this bias can be eliminated by sufficient observational coverage and relatively few of the planets already detected should suffer from this effect (D. Fischer, private communication). The eccentricities of multiple planet systems can also vary with time through secular interactions (analogous to the secular eccentricity variations of Jupiter and Saturn). The observed eccentricity distribution of the extrasolar planets is thus a particular sampling of a larger underlying distribution. The observed eccentricity values can be either lower or higher than the mean values sampled over a secular cycle; although this effect can influence the interpretation of a particular eccentricity value, it will not affect the overall distribution of eccentricity of interest here.

4.2. Additional Evolution of the Orbital Elements

The orbital elements of the planets will, in general, continue to evolve after the end of the simulations presented in the previous section. In order to compare the theoretical results of this migration scenario with the orbital elements of observed extrasolar planets, this additional evolution should be taken into account. In this section we discuss two physical processes – continued orbital evolution driven by the circumstellar disk (with time scale ~ 1 Myr) and longer term circularization due to interactions of close planets with the star (with time scale ~ 1 Gyr).

The simulations end when a planet is ejected or accreted, a collisions take place, or after a fiducial time span of 1 Myr. In general, however, the disk will not lose its ability to drive migration at exactly the same time that the simulations are stopped. Suppose that the disk continues to drive Type II migration (and eccentricity damping) over a time span Δt . The orbital elements will evolve from their values (a_0, ϵ_0) at the end of the numerical simulations to new values given by

$$a_f = a_0 e^{-\Delta t/\tau_{\text{damp}}} \quad \text{and} \quad \epsilon_f = \epsilon_0 e^{-\Delta t/\tau_{\text{ed}}} . \quad (9)$$

Since the migration time τ_{damp} and eccentricity damping time τ_{ed} are determined for a given simulation, the distribution of values for the additional migration time Δt determines the final distribution of orbital elements.

Unfortunately, the correct choice of the Δt distribution is not known. The numerical experiments begin with the planets already formed, so the disk has already been around for some time before the clock starts, and this lead time will vary from system to system. In fact, within the core accretion scenario of planet formation, theories often have trouble forming giant planets while the disk retains its gas (e.g., Kornet et al. 2002 suggest a formation time of about 3 Myr), which leaves little time for migration. The planets with the largest masses in our numerical simulations lead to the shortest integration times, but these same planets are expected to have the longest formation times. Astronomical observations show that circumstellar disks have lifetimes in the range 3 – 6 Myr (e.g., Haisch et al. 2001), significantly longer than the ~ 1 Myr time spans of the integrations. However, this range of observed disk lifetimes represents the time span over which the disk exhibits

observational signatures. The time over which the disk is sufficiently massive to drive (Type II) planet migration will be significantly shorter. In light of these uncertainties, this paper explores a set of algorithms to account for additional evolution of the orbital elements by the disk, i.e., a set of simple, but well-defined, distributions for the remaining migration time Δt . These distributions and their effects on the orbital elements are described in the following subsection.

The system evolution discussed thus far produces orbital elements that apply to system ages of a few Myr, immediately after planets have finished forming and the disk has lost its ability to drive migration. Longer term evolution can also take place. On time scales $\sim 1 - 6$ Gyr characteristic of the stellar ages in observed extrasolar planetary systems, tidal interactions with the star act to circularize close orbits. In the absence of other processes, the eccentricity of a planetary orbit decays with a time scale $\tau_{\text{circ}} = -\epsilon/\dot{\epsilon}$. Here we write this time scale in an approximate form (see Goldreich and Soter 1966; Hut 1981; Wu and Goldreich 2002):

$$\tau_{\text{circ}} \approx \frac{2}{21} \frac{Q}{k_2} \left(\frac{a^3}{GM_*} \right)^{1/2} \frac{m_P}{M_*} \left(\frac{a}{R_P} \right)^5 (1 - \epsilon^2)^{13/2} [f(\epsilon^2)]^{-1}, \quad (10)$$

where $Q \approx 10^5 - 10^6$ is the tidal quality factor, $k_2 \approx 1/2$ is the tidal Love number, and $R_P \approx R_J \approx 7 \times 10^9$ cm is the radius of the planet (notice that this radius is smaller than that used for the collision cross section in the simulations because the planets will contract over the longer time spans considered here). This form includes the essential dependence of the circularization time scale on eccentricity, where $f(\epsilon^2)$ is a rather complicated function of ϵ (defined by eqs. [9–12] of Hut 1981). Evaluation of this time scale for representative values of the parameters indicates that

$$\tau_{\text{circ}} \approx 1\text{Gyr} \left[a/(0.05 \text{ AU}) (1 - \epsilon^2) \right]^{13/2} [f(\epsilon^2)]^{-1}. \quad (11)$$

As a result, orbits with $a \leq 0.05$ AU are expected to be (nearly) circularized, and orbits with somewhat larger a will experience a substantial decrease in eccentricity. Although a number of additional processes can take place (e.g., orbital decay and stellar spinup – see Lin et al. 2000), the leading order effect is loss of eccentricity at constant angular momentum (see also Goldreich and Soter 1966; Hut 1981; Wu and Goldreich 2002). Here we numerically integrate the (nonlinear) evolution equation for eccentricity over the stellar ages t_* , which are assumed to lie in the range $t_* = 1 - 6$ Gyr. In the following subsection, we apply this correction to the theoretical data set in order to compare with observations, although only the closest orbits are affected.

4.3. Comparison of Theory and Observation

One way to evaluate the effectiveness of this migration mechanism is to compare the resulting two-dimensional distribution of orbital elements in the $a - \epsilon$ plane with those of the observed extrasolar planets. This subsection presents such a comparison in systematic fashion. For all cases discussed here, we use the log-random IMF, as it closely mirrors the observed mass distribution of extrasolar planets. The number of theoretical planets is taken to be equal to the number in

the observed sample, where the theoretical planets are chosen randomly from the ensemble of simulations. We then produce $a - \epsilon$ diagrams for each value of the eccentricity damping time scale $\tau_{\text{ed}} = 0.1, 0.3, 1.0$ Myr, and $\tau_{\text{ed}} \rightarrow \infty$. Within this format, the results are presented for a collection of possible corrections for additional evolution of the orbital elements and selection effects, as outlined above.

The first comparison is shown in Fig. 9, which shows the $a - \epsilon$ plane for observed and theoretical planets, with no corrections applied for possible additional evolution. The location of the observed extrasolar planets in the $a - \epsilon$ plane are marked by the star symbols, whereas the results of the theoretical simulations are marked by open squares. The four panels show the results of the four eccentricity damping time scales. The theoretical distribution of planets moves to lower values of eccentricity and to lower values of semi-major axis as the eccentricity damping time scale decreases. The lower ϵ values are a direct result of the increased effectiveness of eccentricity damping. The lower values of a occur because the increased eccentricity damping keeps the planets stable for longer times and the disk has more time to move planets inward. This figure suggests that the simulations with no eccentricity damping ($\tau_{\text{ed}} \rightarrow \infty$; lower right panel) produce too many high eccentricity planets compared to the observational sample, whereas the simulations with $\tau_{\text{ed}} = 0.1$ Myr (upper left panel) tend to produce planetary orbits with too little eccentricity. Nonetheless, the zeroth order result of this comparison is that both the observed planets and the theoretical simulations fill most of the $a - \epsilon$ plane shown here (except for the case $\tau_{\text{ed}} \rightarrow \infty$, which ejects planets before they move far enough inward). Nonetheless, some differences appear, and we need to explore whether or not the corrections for additional evolution described above act to bring the observational and theoretical samples into better agreement.

The discussion of Section 4.1 suggests that the observed sample is likely to be incomplete for planet masses below $0.5 m_J$, with the level of incompleteness increasing with semi-major axis a . In other words, the sample is incomplete for small values of the reflex velocity k_{re} . To determine the importance of this issue on our assessment of this migration mechanism, we present the same set of $a - \epsilon$ diagrams with a k_{re} cut applied; specifically, all planets in the theoretical sample with $k_{\text{re}} \leq 3$ m/s have been removed from consideration. The result is shown in Fig. 10. No other corrections for additional evolution have been applied to the theoretical sample. Comparison of Figs. 9 and 10 indicates that mass/ k_{re} incompleteness has only a modest effect on comparisons of the $a - \epsilon$ plane. This result makes sense because the mass range in question, roughly $m_P \leq 0.5 m_J$, represents about one fourth of the starting mass range, but relatively more of the low mass planets are ejected or accreted (see Fig. 7 and Table 2). As a result, only 10 – 15 percent of the surviving planets fall in this low mass range.

In order to take into account additional evolution of the orbital elements beyond the end of the simulations due to the surviving circumstellar disk, we apply corrections according to equation (9). As discussed above, the distribution of additional migration time Δt is not well determined. As a result, we explore different algorithms for continued evolution. In the first case, we assume that the disk is able to drive migration beyond the end of the numerical simulations for an additional

time given by $\Delta t = \delta t - t_{sim}$, where t_{sim} is the time at the end of the simulation, δt is a random time scale in the range 0 – 1 Myr (where negative values of Δt are set to zero, i.e., no additional evolution). This is the same algorithm used in the previous study of this migration scenario in AL2003. The resulting $a - \epsilon$ diagrams are shown in Fig. 11 for different choices of eccentricity damping time scale. The continued migration moves the points to lower values of both a and ϵ , and the random time element tends to spread the distributions, although the effect is relatively small (except for the case with no eccentricity damping). Nonetheless, this correction acts to bring the theoretical and observational distributions into closer agreement (although the distribution of Δt applied here is not unique).

An alternate assumption for additional evolution is that the disk has a remaining lifetime Δt that is random and independent of the previous evolution. Keep in mind that Δt is the time over which the disk has enough mass to change the orbital elements of any remaining planets; the disk may exhibit observational signatures over longer times. Fig. 12 shows the resulting $a - \epsilon$ diagrams for random disk lifetimes in the range $\Delta t = 0 - 0.3$ Myr. Fig. 13 shows the $a - \epsilon$ diagrams for random disk lifetimes in the somewhat longer range $\Delta t = 0 - 0.5$ Myr. These results are much the same as for the previous algorithm illustrated in Fig. 11. Any similar model of continued disk evolution will move the theoretical points to smaller values of (a, ϵ) and will spread the distributions. The magnitude of the effect (the mean value of the Δt distribution) matters more than the particular choice of algorithm (which sets the shape of the distribution). Inspection of Figs. 11 – 13 suggests that a mean value $\langle \Delta t \rangle \approx 0.3 - 0.5$ Myr is needed to provide reasonable agreement with observations. Notice that the model allows for some interplay between this time scale and the eccentricity damping time scale – for larger τ_{ed} , less additional evolutionary time $\langle \Delta t \rangle$ is indicated.

Next we consider corrections to the orbital elements due to the longer term process of tidal circularization by the central star. To account for this effect, we integrate the differential equation $\dot{\epsilon}/\epsilon = -\tau_{circ}^{-1}$, with the circularization time scale given by equations (10, 11). The assumed system lifetimes are assumed to be randomly distributed and lie in the range 1 – 6 Gyr, similar to the stellar ages in the observed sample. The resulting $a - \epsilon$ diagrams are shown in Fig. 14. The inclusion of this circularization processes cleans up an important discrepancy between the theoretical and observed orbital elements, namely the observed lack of short period planets (small a) with substantial eccentricities.

Finally, in Fig. 15, we present a set of $a - \epsilon$ diagrams with all of the corrections applied: a reflex velocity cut such that only planets with $k_{re} > 3$ m/s remain, continued migration with remaining disk lifetimes given by the algorithm depicted in Fig. 11, and the circularization correction. The resulting theoretical distributions of a and ϵ are in reasonable agreement with those of the observed sample of extrasolar planets. The eccentricity damping time scale $\tau_{ed} = 0.3$ Myr (i.e., $\tau_{ed} = \tau_{damp}$) provides the best fit, although all three cases with τ_{ed} in the range 0.3 – 3 Myr are in the right ballpark.

5. Conclusion

This paper explores a migration scenario in which multiple giant planets are driven inward through the action of tidal torques in a circumstellar disk. In this case, the outer planet interacts with the disk, which drains energy and angular momentum away from the planetary orbit. As the outer planet migrates inward, it eventually becomes close enough to the interior planet to force it inward and to drive eccentricity growth with increasingly violent interactions. Such systems are generally not stable in the long term and adjust themselves to stability by ejecting a planet, accreting a planet onto the central star, or by having the two planets collide. The surviving planet is left on an eccentric orbit of varying semi-major axis, roughly consistent with the orbits of observed extrasolar planets. On longer time scales, tidal interactions with the central star act to circularize the orbits of the closet planets. We have presented a comprehensive, but not exhaustive, exploration of parameter space for this migration scenario. Our main results can be summarized as follows:

[1] This migration scenario results in a wide variety of final systems with a broad distribution of orbital elements. In particular, this migration scenario can fill essentially the entire $a - \epsilon$ plane for semi-major axes a smaller than the initial values. The observed extrasolar planets have orbital elements that fill the $a - \epsilon$ plane in roughly the same way (see Figs. 9 – 15). When the theoretical ensemble of planets is corrected for additional orbital evolution due to interactions with the circumstellar disk (on ~ 1 Myr time scales) and tidal interactions with the central star (on ~ 1 Gyr time scales), the resulting distributions of theoretical orbital elements are in reasonable agreement with those of the observed sample of extrasolar planets.

[2] Planets of smaller mass tend to be the ones that are ejected or accreted (see Figs. 3 and 4). The mass distribution of the observed planetary sample is roughly log-random, with a moderate deficit of planets at the low mass end (Fig. 7). This shape is consistent with planets being formed with (roughly) a log-random mass distribution and the lower end of the mass function being depleted through planet-planet scattering, as produced by this migration mechanism. Keep in mind, however, that the lower end of the mass distribution also suffers from selection effects (Tabachnik and Tremaine 2002), which must be sorted out before definitive conclusions can be made (see Section 4.1).

[3] The mutual gravitational interactions of the planets are highly effective at increasing orbital eccentricities. The general trend is for planet-planet scattering to produce orbital eccentricities that are somewhat larger than those observed in the current sample of extrasolar planets. As a result, real solar systems must either provide sufficient eccentricity damping as suggested by numerical simulations of planet-disk interactions (e.g., Kley et al. 2004; Nelson et al. 2000), contain only single planets, or provide a mechanism to keep multiple planets sufficiently separated. The eccentricity damping time scale that provides the best fit to the observations lies in the range $\tau_{\text{ed}} = 0.1 - 1$ Myr for a viscous damping time scale of $\tau_{\text{damp}} = 0.3$ Myr, i.e., the ratio $\tau_{\text{ed}}/\tau_{\text{damp}} = 1/3 - 3$.

[4] The inclination angles of the planetary orbits are excited with a well-defined distribution centered of $\Delta i \approx 5$ degrees (Figs. 6 and 7). For the end states of this migration mechanism, the

inclination angle excitation is correlated with the excitation of orbital eccentricity (Table 6).

[5] This migration scenario leads to a large number of ejected planets; specifically, about one-third to one-half of the simulated systems eject a planet. The distribution of ejection speeds is broad, with a peak near 5 km/s and a long tail toward higher speeds (Fig. 8). The functional form of the distribution of ejection speeds can be understood in terms of the simple physical argument given in Section 3.5. More than 90 percent of the exiled planets are predicted to attain ejection speeds greater than 1 km/s, the speed required for planets to (immediately) escape their birth aggregate. As a result, typical stellar birth clusters (with $N_* \approx 300$) are expected to contain only ~ 12 free floating planets at a given time due to this migration mechanism.

This migration scenario produces a full distribution of orbital elements for the surviving planets and is in reasonable agreement with observations. In order for this mechanism to be successful, the systems must have a number of properties, and it is useful to summarize them here: The planets that end up in the currently observed region of the $a - \epsilon$ plane are assumed to have formed in disk annulus $r = 3 - 7$ AU, roughly where Jupiter lives in our solar system. The disk must be able to sustain Type II migration torques over time scales ~ 1 Myr; the disk must maintain more mass (in gas) than its planets over this time scale, which is comparable to the time required for giant planets to form through the core accretion mechanism. Some system-to-system variation in this migration time scale is also indicated. As mentioned above, disk signatures are observed over longer times (several Myr), although the disks do not necessarily maintain enough mass to drive migration over this longer time. The torques must be large enough so that $|a/\dot{a}| \approx 0.3$ Myr, which is equivalent to having a viscosity parameter $\alpha \sim 10^{-3}$. The disk must damp orbital eccentricity of the outer planet with a damping time scale in the range 0.1 – 1 Myr (so that $|\epsilon\dot{a}/\dot{\epsilon}a| \sim 1$). The planetary IMF must be nearly log-random, more specifically, close to the observed planetary mass function with a moderate excess of lower mass planets (they are the ones accreted or ejected). Finally, in order to not overpopulate the (low a , high ϵ) portion of parameter space, close orbits must be circularized and hence the tidal quality factor must lie in the estimated range $Q = 10^5 - 10^6$. If the system parameters differ significantly from these values/ranges, then this migration mechanism (in the form studied here) will not produce the observed orbital elements of extrasolar planets.

Although this migration mechanism is promising, a number of issues remain unresolved and should be considered in future work. One important issue is the manner in which eccentricity is damped by the circumstellar disk. The parametric treatment presented here indicates that in order for the theory to produce results consistent with the observed distributions of orbital elements, the ratio of the eccentricity damping time scale to the migration (disk accretion) time scale should lie in the range $\tau_{\text{ed}}/\tau_{\text{damp}} \approx 1/3 - 3$. Numerical simulations of circumstellar disks interacting with planets often provide a damping time scale near the low end of this range (e.g., Nelson et al. 2000, Kley et al. 2004), whereas competing analytic calculations suggest that eccentricity is not damped at all, but rather is excited by the disk (Goldreich and Sari 2003, Ogilvie and Lubow 2003). Since a particular disk cannot damp and excite eccentricity at the same time, these two conflicting results define an interesting problem for future study. The resolution of this issue must allow for

eccentricity damping time scales in the proper range ($\tau_{\text{ed}}/\tau_{\text{damp}} \approx 1/3-3$) if this migration scenario represents the correct explanation for the observed extrasolar planetary orbits.

The most fundamental challenge for the future is to determine which migration scenario (or scenarios) acts to produce the observed orbits of extrasolar planets. Any viable migration scenario must be able to explain the observed distributions of orbital elements. This paper shows that Type II migration (modeled using parametric disk torques) acting in combination with planet-planet scattering can produce these observed distributions, but perhaps other mechanisms will also prove to be successful – there is not a uniqueness theorem for this problem. Discriminating among mechanisms might therefore rely on secondary predictions. Although the full consequences of the various migration mechanisms have not been worked out, some preliminary statements can be made: For example, if scattering processes play a role in planet migration, then the scattering bodies will often be ejected. More scattering leads to more ejected bodies. The scenario considered here (planet-planet scattering combined with Type II migration through a circumstellar disk) implies that about one third of the solar systems will eject a planet with (roughly) one Jovian mass. For scenarios in which a circumstellar disk provides the required eccentricity excitation but multiple planets are present, planet-planet interactions tend to excite additional eccentricity and planets are more readily ejected. As a specific example, we ran an additional set of 375 simulations with the log-random IMF, $\tau_{\text{damp}} = 0.3$ Myr, and $\tau_{\text{ed}} = -1$ Myr (corresponding to eccentricity excitation); we found that 100% of the systems ejected one of the planets so that no multiple planet systems remained. For scenarios in which migration is driven by scattering processes only, even more ejections are predicted. For example, in the case of ten planet systems (AL2003), each solar system ejects 8 or 9 planets with (roughly) Jovian characteristics. If the scattering bodies are planetesimals (Murray et al. 1998), then each solar system would eject several Jupiter masses worth of scattering bodies, but they would be in rocky form. Thus, the currently discussed migration mechanisms provide differing amounts of scattered debris. In the future, additional signatures that discriminate between the various migration scenarios should be identified and developed.

Acknowledgments

We would like to thank Paul Butler, Gus Evrard, Debra Fischer, Greg Laughlin, Man Hoi Lee, and Steve Lubow for beneficial discussions. We also thank the referees for their many useful comments that improved the paper. This work was supported at the University of Michigan by the Michigan Center for Theoretical Physics and by NASA through the Terrestrial Planet Finder Mission (NNG04G190G) and the Astrophysics Theory Program (NNG04GK56G0).

REFERENCES

- Adams, F. C., Laughlin, G., 2003. Migration and dynamical relaxation in crowded systems of giant planets. *Icarus* 163, 290 – 306 (AL2003).
- Bate, M. R., Lubow, S. H., Ogilvie, G. I., Miller, K. A., 2003. Three-dimensional calculations of high- and low-mass planets embedded in protoplanetary discs. *Mon. Not. R. Astron. Soc.* 341, 213 – 229.
- Beaugé, C., Ferraz-Mello, S., Michtchenko, T. A., 2003. Extrasolar planets in mean-motion resonance: Apes alignment and asymmetric stationary solutions. *Astrophys. J.* 593, 1124 – 1133.
- Bernstein, R., Shtetman, S. A., Gunnels, S. M., Mochnacki, S., Athey, A. E., 2003. MIKE: A Double Echelle spectrograph for the Magellan Telescopes at Las Campanas Observatory. *SPIE* 4841, 1694 – 1704.
- Bryden, J., Rózycka, M., Lin, D.N.C., Bodenheimer, P. 2000. On the interaction between protoplanets and protostellar disks. *Astrophys. J.* 540, 1091 – 1101.
- Ferraz-Mello, S., Beaugé, C., Michtchenko, T. A., 2003. Evolution of Migrating Planet Pairs in Resonance. *Celest. Mech. Dynam. Astron.* 87, 99 – 112.
- Fischer, D. A., Marcy, G. W., Butler, R. P., Vogt, S. S., Frink, S., Apps, K. 2001. Planetary Companions to HD 12661, HD 92788, and HD 38529 and Variations in Keplerian Residuals of Extrasolar Planets. *Astrophys. J.* 551, 1107 – 1118.
- Ford, E. B., Havlickova, M., Rasio, F. A., 2001. Dynamical instabilities in extrasolar planetary systems containing two planets. *Icarus* 150, 303 – 313.
- Goldreich, P., Sari, R., 2003. Eccentricity evolution for planets in gaseous disks. *Astrophys. J.* 585, 1024 – 1037.
- Goldreich, P., Soter, S., 1963. Q in the solar system. *Icarus* 5, 375 – 389.
- Goldreich, P., Tremaine, S., 1980. Disk-satellite interactions. *Astrophys. J.* 241, 425 – 441.
- Haisch, K. E., Lada, E. A., Lada, C. J., 2001. Disk frequencies and lifetimes in young clusters. *Astrophys. J.* 553, L153 – 156.
- Hatzes, A. P., and 12 colleagues, Evidence for a long period planet orbiting Epsilon Eridani. *Astrophys. J.* 529, L145 – 148.
- Hut, P., 1981. Tidal evolution in close binary systems. *Astron. Astrophys.* 99, 126 – 140.
- Katz, J. I., 1997. Single close encounters do not make eccentric planetary orbits. *Astrophys. J.* 484, 862 – 865.

- Kley, W., 1999. Mass flow and accretion through gaps in accretion discs. *Mon. Not. R. Astron. Soc.* 303, 696 – 710.
- Kley, W., 2000. On the migration of a system of protoplanets. *Mon. Not. R. Astron. Soc.* 313, L47 – L51.
- Kley, W., D’Angelo, G., Henning, T., 2001. Three-dimensional simulations of a planet embedded in a protoplanetary disk. *Astrophys. J.* 547, 457 – 464.
- Kley, W., Peitz, J., Bryden, G., 2004. Evolution of planetary systems in resonance. *Astron. Astrophys.* 414, 735 – 747.
- Kornet, K., Bodenheimer, P., Rózyczka, M., 2002. Models of the formation of the planets in the 47 UMa system. *Astron. Astrophys.* 396, 977 – 986.
- Lada, C. J., Lada, E. A., 2004. Embedded clusters in molecular clouds. *Ann. Rev. Astron. Astrophys.* 41, 57 – 115.
- Laughlin, G., Chambers, J. E., Fischer, D., 2002. A dynamical analysis of the 47 Ursae Majoris planetary system. *Astrophys. J.* 579, 455 – 467.
- Lee, M. H. 2004. Diversity and origin of 2:1 orbital resonances in extrasolar planetary systems. *Astrophys. J.* 611, 517 – 527.
- Lee, M. H., Peale, S. J., 2002. Dynamics and origin of the 2:1 orbital resonances of the GJ 876 planets. *Astrophys. J.* 567, 596 – 609.
- Lin, D.N.C., Bodenheimer, P., Richardson, D. C., 1996. Orbital migration of the planetary companion of 51 Pegasi to its present location. *Nature* 380, 606 – 607.
- Lin, D.N.C., Ida, S., 1997. On the origin of massive eccentric planets. *Astrophys. J.* 477, 781 – 791.
- Lin, D.N.C., Papaloizou, J.C.B., 1993. On the tidal interaction between protostellar disks and companions. in *Protostars and Planets III*, eds. E. H. Levy and J. I. Lunine. (Tucson: Univ. Arizona Press), pp. 749 – 836.
- Lin, D.N.C., Papaloizou, J.C.B., Terquem, C., Bryden, G., Ida, S. 2000. Orbital evolution and planet-star interaction. in *Protostars and Planets IV*, eds. V. Mannings, A. P. Boss, and S. S. Russell. (Tucson: Univ. Arizona Press), pp. 1111 – 1134.
- Lubow, S. H., Ogilvie, G. I., 2001. Secular interactions between inclined planets and a gaseous disk. *Astrophys. J.* 560, 997 – 1009.
- Marcy, G. W., Butler, R. P., 1996. A planetary companion to 70 Virginis. *Astrophys. J.* 464, L147 – 150.

- Marcy, G. W., Butler, R. P., 1998. Detection of extrasolar giant planets. *Ann. Rev. Astron. Astrophys.* 36, 57 – 97.
- Marcy, G. W., Butler, R. P., 2000. Planets orbiting other suns. *Publ. Astron. Soc. Pacific* 112, 137 – 140.
- Marzari, F., Weidenschilling, S. J., 2002. Eccentric extrasolar planets: The jumping Jupiter model. *Icarus* 156, 570 – 579.
- Masset, F. S., Papaloizou, J.C.B., 2003. Runaway migration and the formation of hot Jupiters. *Astrophys. J.* 588, 494 – 508.
- Masset, F. S., Snellgrove, M., 2001. Reversing type II migration: resonance trapping of a lighter giant protoplanet. *Mon. Not. R. Astron. Soc.* 320, L55 – 59.
- Mayor, M., Queloz, D., 1995. A Jupiter-mass companion to a solar-type star. *Nature* 378, 355 – 359.
- Murray, C. D., Dermott, S. F., 2001. *Solar System Dynamics*. (Cambridge: Cambridge Univ. Press).
- Murray, N., Hansen, B., Holman, M., Tremaine, S., 1998. Migrating Planets. *Science* 279, 69 – 71.
- Murray, N., Paskowitz, M., Holman, M., 2002. Eccentricity evolution of migrating planets. *Astrophys. J.* 565, 608 – 620.
- Naef, D., and 11 colleagues, 2001. HD80606b, A planet on an extremely elongated orbit. *Astron. Astrophys.* 375, L27 – 30.
- Nelson, R. P., Papaloizou, J.C.B., Masset, F., Kley, W., 2000. The migration and growth of protoplanets in protostellar discs. *Mon. Not. R. Astron. Soc.* 318, 18 – 36.
- Ogilvie, G. I., Lubow, S. H., 2003. Saturation of the corotation resonance in a gaseous disk. *Astrophys. J.* 587, 398 – 406.
- Papaloizou, J.C.B., 2003. Disc-Planet Interactions: Migration and resonances in extrasolar planetary systems. *Celest. Mech. Dynam. Astron.* 87, 53 – 83.
- Papaloizou, J.C.B., Nelson, R. P., Masset, E., 2001. Orbital eccentricity growth through disc-companion tidal interaction. *Mon. Not. R. Astron. Soc.* 366, 263 – 275.
- Papaloizou, J.C.B., Terquem, C., 2001. Dynamical relaxation and massive extrasolar planets. *Mon. Not. R. Astron. Soc.* 325, 221 – 230.
- Perryman, M.A.C., 2000. Extra-solar planets. *Inst. Phys. Rep. Progress Phys.* 63, 1209 – 1272.
- Porras, A., Christopher, M., Allen, L., Di Francesco, J., Megeath, S. D., Myers, P. C., 2003. A catalog of young stellar groups and clusters within 1 kpc of the Sun. *Astron. J.* 126, 1916 – 1924.

- Press, W. B., Flannery, B. P., Teukolsky, S. A., Vetterling, W. T., 1986. *Numerical Recipes: The art of scientific computing*. (Cambridge: Cambridge Univ. Press).
- Press, W. B., Teukolsky, S. A., 1977. On the formation of close binaries by two-body tidal capture. *Astrophys. J.* 213, 183 – 192.
- Rasio, F. A., Ford, E. B., 1996. Dynamical instabilities and the formation of extrasolar planetary systems. *Science* 274, 954 – 956.
- Schäfer, C., Speith, R., Hipp, M., Kley, W., 2004. Simulations of planet-disc interactions using Smoothed Particle Hydrodynamics. *Astron. Astrophys.* 418, 325 – 335.
- Shu, F. H., 1992. *Gas Dynamics*. (Mill Valley: Univ. Science Books).
- Snellgrove, M. D., Papaloizou, J.C.B., Nelson, R. P., 2001. On disc driven inward migration of resonantly coupled planets with application to the system around GJ876. *Astron. Astrophys.* 374, 1092 – 1099.
- Tabachnik, S., & Tremaine, S. 2002. Maximum-likelihood method for estimating the mass and period distributions of extrasolar planets. *Mon. Not. R. Astron. Soc.* 335, 151 – 158.
- Thommes, E. W., Lissauer, J. J., 2003. Resonant inclination excitation of migrating giant planets. *Astrophys. J.* 597, 566 – 580.
- Trilling, D. E., Benz, W., Guillot, T., Lunine, J. I., Hubbard, W. B., Burrows, A., 1998. Orbital evolution and migration of giant planets: Modeling extrasolar planets. *Astrophys. J.* 500, 902 – 914.
- Ward, W. R., 1997. Protoplanet migration by nebula tides. *Icarus* 126, 261 – 281.
- Ward, W. R., Hahn, J. M. 2000. Disk-Planet Interactions and the Formation of Planetary Systems. in *Protostars and Planets IV*, eds. V. Mannings, A. P. Boss, and S. S. Russell. (Tucson: Univ. Arizona Press), pp. 1135 – 1155.
- Weidenschilling, S. J., Marzari, F., 1996. Gravitational scattering as a possible origin for giant planets at small stellar distances. *Nature* 384, 619 – 620.
- Weinberg, S., 1972. *Gravitation and cosmology*. (New York: Wiley).
- Wu, Y., Goldreich, P., 2002. Tidal evolution of the planetary system HD 83443. *Astrophys. J.* 564, 1024 – 1027.
- Zapatero Osorio, M. R., Bjar, V.J.S., Martn, E. L., Rebolo, R., Barrado y Navascus, D., Bailer-Jones, C.A.L., Mundt, R., 2000. Discovery of young isolated planetary mass objects in the Sigma Orionis star cluster. *Science* 290, 103 – 107.

Table 1: Planetary Fate Probabilities

τ_{ed}	Ejection	Accretion	Collision	Survival
Linear IMF				
0.3 Myr	0.526	0.332	0.031	0.112
1.0 Myr	0.562	0.192	0.006	0.241
3.0 Myr	0.548	0.163	0.003	0.286
Log IMF				
0.1 Myr	0.253	0.402	0.072	0.273
0.3 Myr	0.339	0.347	0.030	0.285
1.0 Myr	0.335	0.294	0.005	0.371
∞	0.348	0.333	0.004	0.295
Log IMF (2:1)				
1.0 Myr	0.288	0.349	0.011	0.352

Table 2: Planet Masses (in m_J)

τ_{ed}	Ejectors	Ejectees	Accreted	Accretion Survivor	2-Planet Systems
Linear IMF					
0.3 Myr	3.67 ± 0.88	2.53 ± 1.36	1.01 ± 0.64	3.29 ± 1.08	1.27 ± 0.76
1.0 Myr	3.56 ± 0.96	2.21 ± 1.38	0.79 ± 0.65	3.25 ± 1.11	1.83 ± 1.11
3.0 Myr	3.47 ± 0.93	2.22 ± 1.51	0.65 ± 0.54	3.43 ± 1.06	1.76 ± 0.98
Log IMF					
0.1 Myr	5.73 ± 1.89	1.60 ± 1.88	0.92 ± 1.04	3.25 ± 2.72	0.80 ± 0.82
0.3 Myr	5.19 ± 2.35	1.75 ± 2.06	0.60 ± 0.61	3.90 ± 2.75	0.69 ± 0.69
1.0 Myr	4.92 ± 2.47	1.80 ± 2.08	0.51 ± 0.51	3.95 ± 2.70	0.78 ± 0.71
∞	5.03 ± 2.42	1.75 ± 1.93	0.45 ± 0.44	3.71 ± 2.84	0.87 ± 0.97
Log IMF (2:1)					
1.0 Myr	4.81 ± 2.16	1.62 ± 2.23	0.65 ± 0.91	3.78 ± 2.60	0.78 ± 0.74

Table 3: Semi-major Axes of Remaining Planets (in AU)

τ_{ed}	Ejectors	Accretion Survivor	2-Planet Systems	All Survivors
Linear IMF				
0.3 Myr	2.26 ± 1.75	0.18 ± 0.22	0.42 ± 0.41	1.22 ± 1.24
1.0 Myr	2.50 ± 2.69	0.70 ± 1.58	0.37 ± 0.34	1.37 ± 0.53
3.0 Myr	2.29 ± 1.11	1.00 ± 1.10	0.60 ± 0.44	1.37 ± 0.87
Log IMF				
0.1 Myr	3.10 ± 6.18	0.21 ± 1.36	0.45 ± 0.44	0.97 ± 3.05
0.3 Myr	2.48 ± 0.94	0.23 ± 0.36	0.41 ± 0.44	0.90 ± 0.60
1.0 Myr	2.62 ± 2.68	0.62 ± 0.60	0.53 ± 0.44	1.05 ± 1.38
∞	2.68 ± 1.89	1.46 ± 0.91	1.26 ± 0.68	1.69 ± 1.18
Log IMF (2:1)				
1.0 Myr	2.61 ± 0.94	0.53 ± 0.88	0.49 ± 0.39	0.95 ± 0.69

Table 4: Eccentricities of Remaining Planets

τ_{ed}	Ejectors	Accretion Survivor	2-Planet Systems	All Survivors
Linear IMF				
0.3 Myr	0.46 ± 0.28	0.28 ± 0.22	0.46 ± 0.25	0.41 ± 0.26
1.0 Myr	0.43 ± 0.26	0.45 ± 0.29	0.68 ± 0.19	0.53 ± 0.24
3.0 Myr	0.40 ± 0.27	0.43 ± 0.32	0.79 ± 0.14	0.58 ± 0.23
Log IMF				
0.1 Myr	0.24 ± 0.25	0.041 ± 0.070	0.30 ± 0.22	0.20 ± 0.19
0.3 Myr	0.25 ± 0.23	0.14 ± 0.18	0.44 ± 0.25	0.31 ± 0.23
1.0 Myr	0.28 ± 0.26	0.34 ± 0.26	0.65 ± 0.22	0.49 ± 0.24
∞	0.29 ± 0.25	0.35 ± 0.35	0.83 ± 0.13	0.55 ± 0.24
Log IMF (2:1)				
1.0 Myr	0.26 ± 0.26	0.38 ± 0.23	0.65 ± 0.21	0.46 ± 0.23

Table 5: Percent of Total Time Spent in 2:1/3:1 Resonances

τ_{damp}	TimeStop	Eject	Accrete	Total	Total(alt)
Linear IMF					
0.3 Myr	47/50	2/83	18/69	22/67	12/73
1.0 Myr	25/72	9/69	20/68	20/70	13/70
3.0 Myr	21/77	11/68	19/67	19/73	13/71
Log IMF					
0.1 Myr	64/32	10/61	40/54	49/44	34/52
0.3 Myr	70/25	8/63	33/46	51/35	33/46
1.0 Myr	70/26	17/55	34/46	55/34	37/44
∞	62/33	15/56	43/37	51/37	32/46
Log IMF (2:1)					
1.0 Myr	100/0	94/0.3	100/0	100/0	94/0.1

Table 6: Linear Correlation Coefficient between ϵ and i

τ_{damp}	Survival	Ejection	Accretion	Total
Linear IMF				
0.3 Myr	0.62 (44)	0.53 (99)	0.61 (96)	0.50 (214)
1.0 Myr	0.064 (260)	0.43 (294)	0.57 (103)	0.31 (660)
3.0 Myr	0.061 (190)	0.39 (180)	0.76 (54)	0.27 (425)
Log IMF				
0.1 Myr	0.69 (428)	0.59 (221)	0.55 (333)	0.64 (1034)
0.3 Myr	0.58 (456)	0.53 (258)	0.57 (274)	0.54 (1013)
1.0 Myr	0.30 (566)	0.56 (248)	0.33 (224)	0.45 (1038)
∞	0.28 (398)	0.40 (228)	0.66 (238)	0.46 (867)
Log IMF (2:1)				
1.0 Myr	0.36 (198)	0.56 (80)	0.60 (98)	0.51 (379)

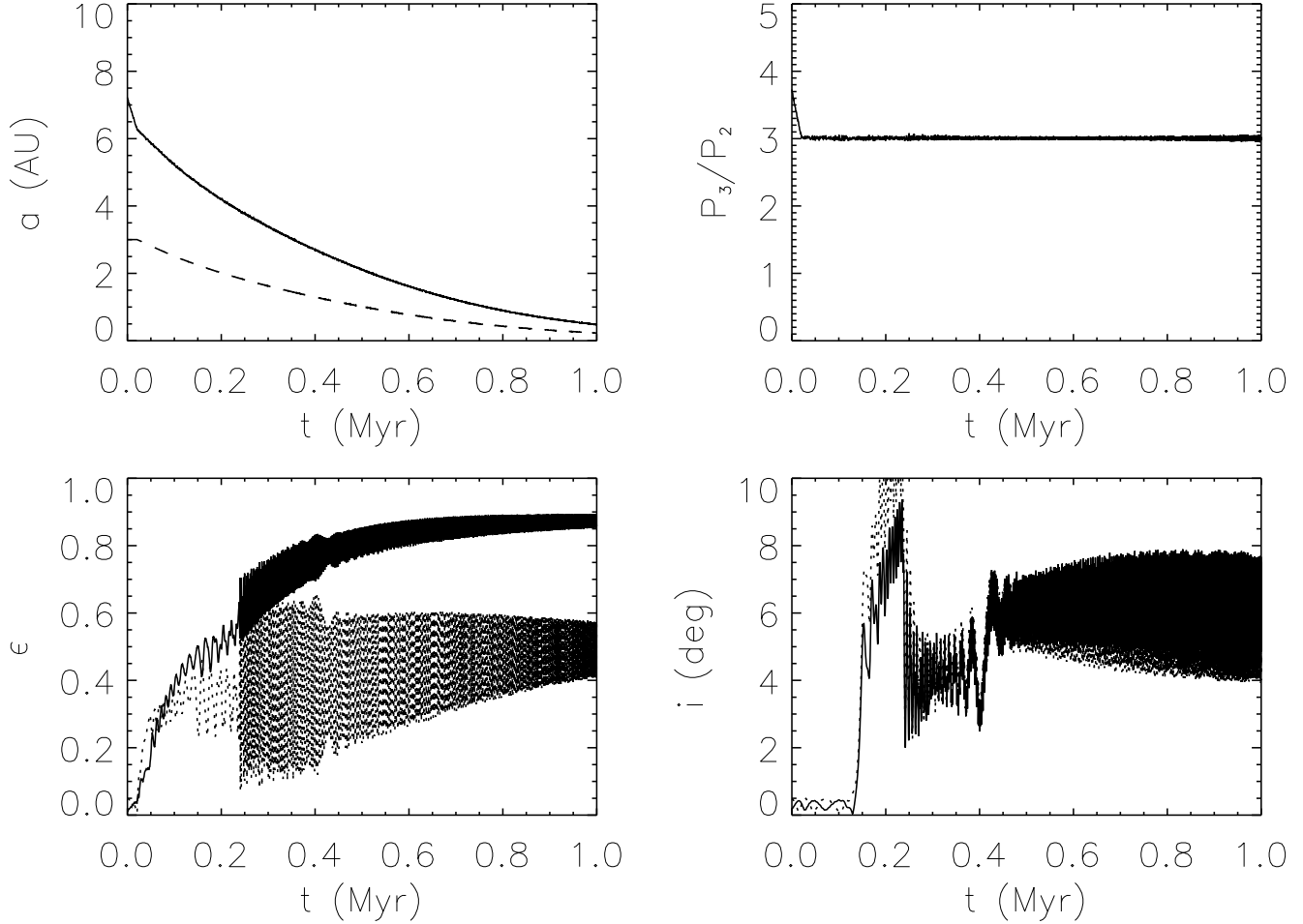


Fig. 1.— Time evolution of a typical system of two interacting planets migrating under the influence of torques from a circumstellar disk. The upper left panel shows the time evolution of the semi-major axes, which decrease steadily on the migration time scale τ_{damp} . The upper right panel shows the ratio of the orbital periods. This ratio quickly decreases to 3 and stays close to this value for much of the evolution (the two planets are near the 3:1 resonance – see section 3.1). The evolution of eccentricity is illustrated in the lower left panel, which shows that the eccentricity of both planets steadily increases at first and then enters into a complicated time series including both short period oscillations and an overall growth trend on longer time scales. The lower right panel shows the corresponding time evolution of the inclination angle. Both planets wander back and forth out of the original orbital plane, but the inclination angles vary by only a few degrees.

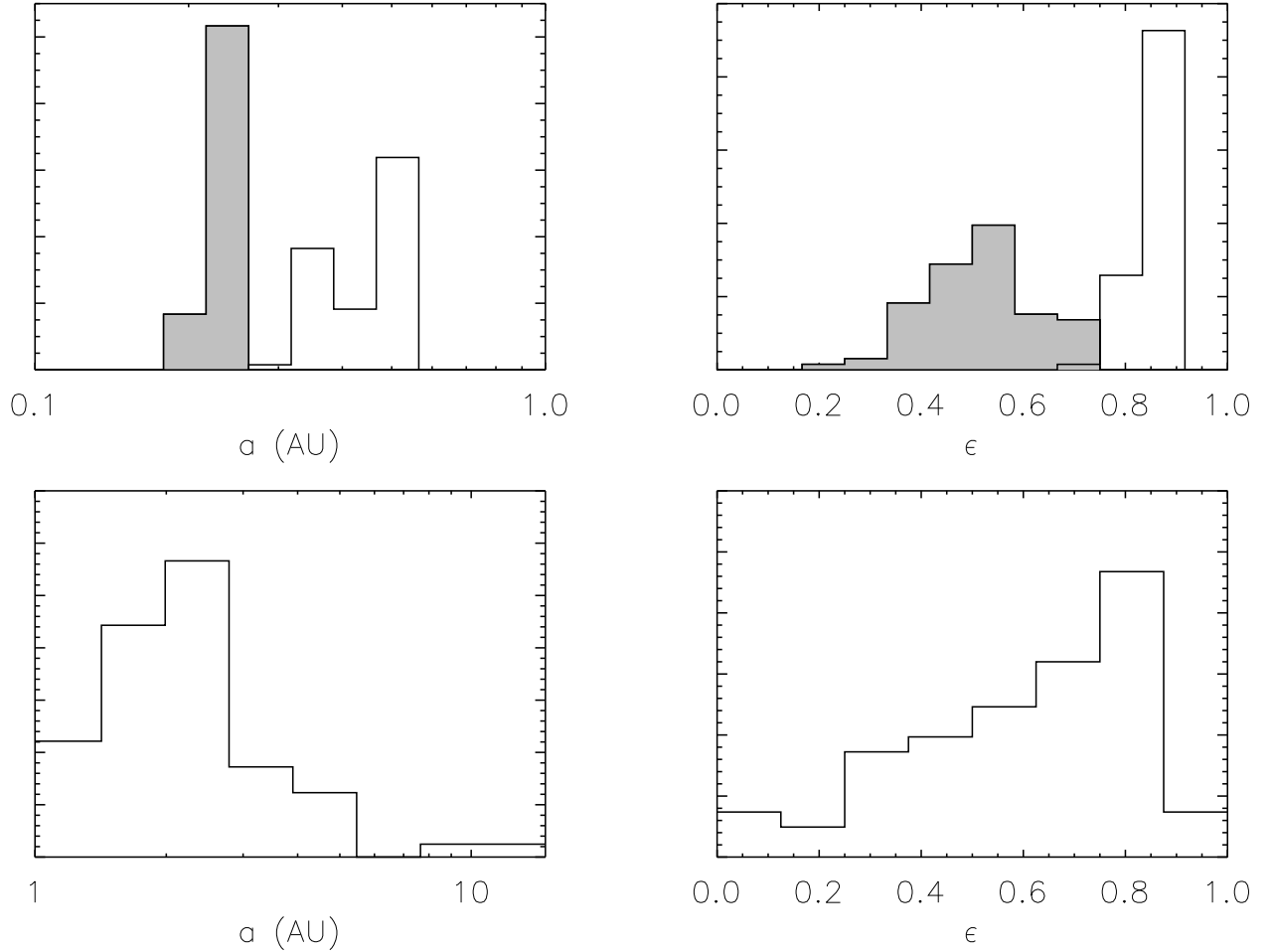


Fig. 2.— Illustration of sensitive dependence on initial conditions. The top panels show the results of simulations performed for two equal mass planets with $m_P = m_J$. The set of simulations use the same starting conditions except for the choice of angular orbital elements. In all cases, both planets survive to the end of the fiducial time period of 1 Myr, but the orbital elements of the planets are different, i.e., they show a distribution of values. The orbital elements of the inner planet are shown as the shaded histogram; those of the outer planet correspond to the unshaded histogram. The bottom two panels show analogous results for simulations done with two equal mass planets with $m_P = 5m_J$. In this case, one of the planets is always ejected, but the remaining planet takes on a distribution of values for its orbital elements.

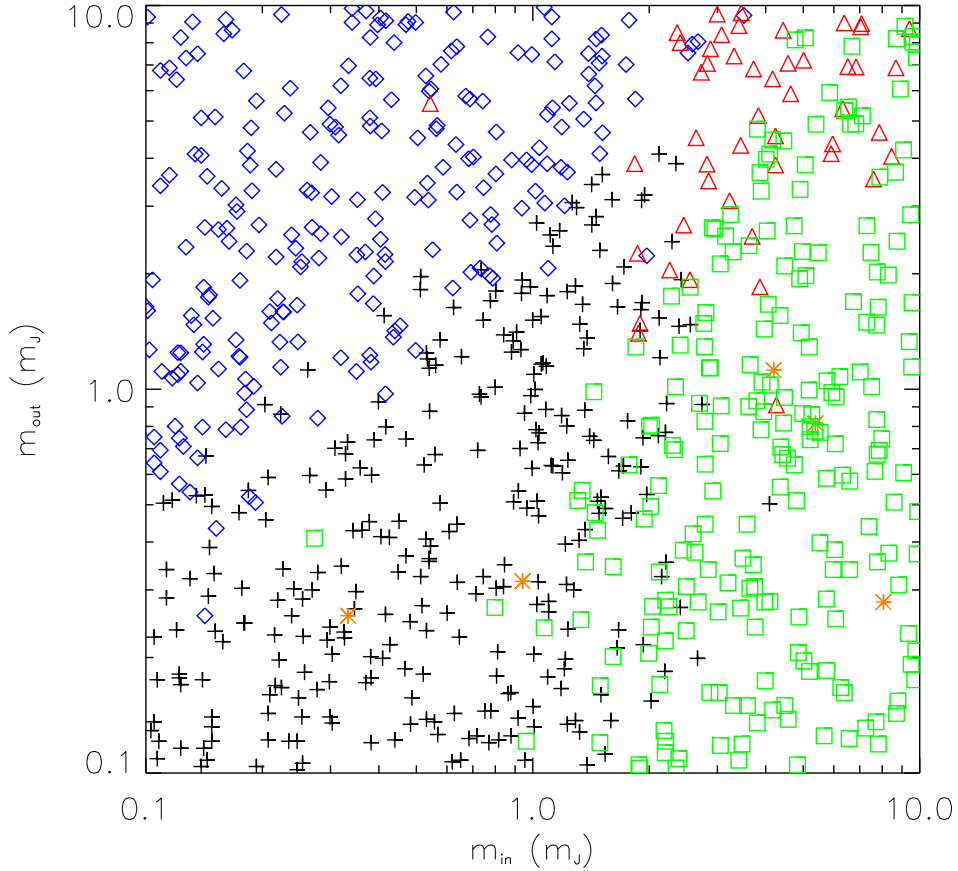


Fig. 3.— End states as a function of the planetary masses for eccentricity damping time scale $\tau_{\text{ed}} = 1$ Myr. Each symbol in this figure represents the outcome of a simulation with the mass of the outer planet plotted as a function of the mass of the inner planet. All of the simulations depicted here use the log-random IMF, the standard starting configuration in which the outer planet begins outside the 3:1 resonance, and eccentricity damping time $\tau_{\text{ed}} = 1$ Myr. The different symbols correspond to different outcomes: open blue diamonds represent accretion of the inner planet, open green squares denote ejection of the outer planet, open red triangles represent ejection of the inner planet, crosses denote survival of both planets, and orange star symbols represent accretion of the outer planet.

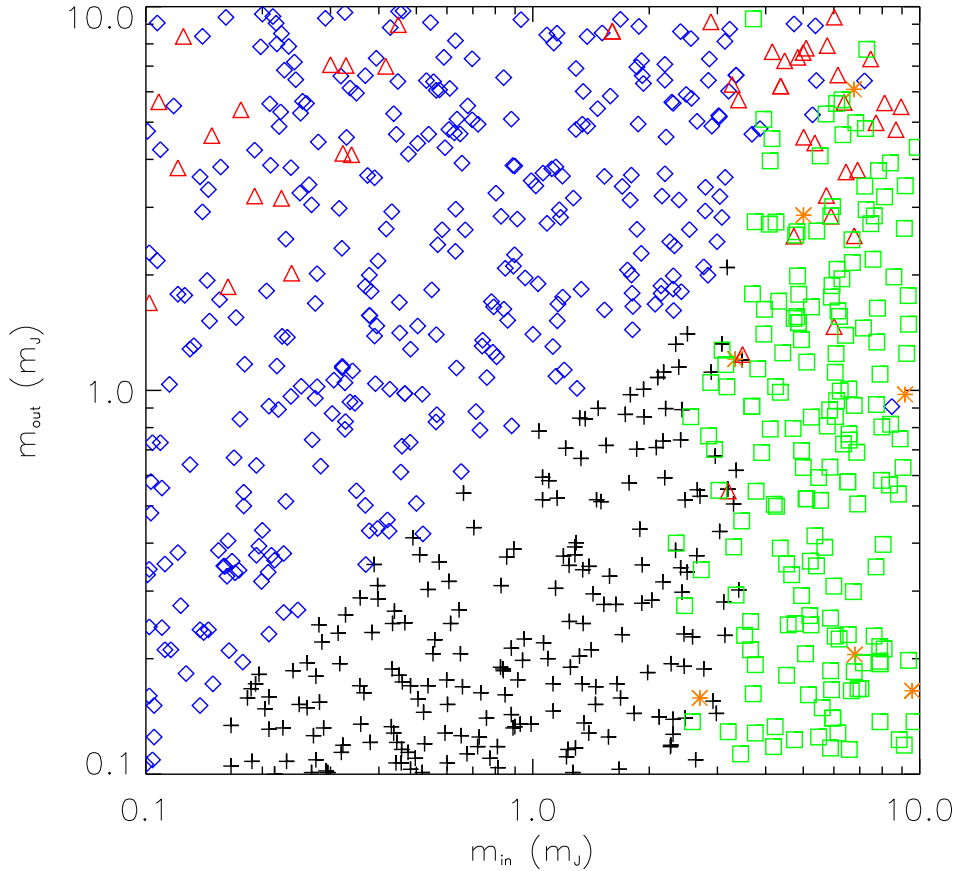


Fig. 4.— End states as a function of the planetary masses for eccentricity damping time scale $\tau_{\text{ed}} = 0.1$ Myr (compare with Fig. 3). Each symbol in this figure represents the outcome of a simulation with the mass of the outer planet plotted as a function of the mass of the inner planet. All of the simulations depicted here use the log-random IMF, the standard starting configuration in which the outer planet begins outside the 3:1 resonance, and eccentricity damping time $\tau_{\text{ed}} = 0.1$ Myr. The different symbols correspond to different outcomes: open blue diamonds represent accretion of the inner planet, open green squares denote ejection of the outer planet, open red triangles represent ejection of the inner planet, crosses denote survival of both planets, and orange star symbols represent accretion of the outer planet.

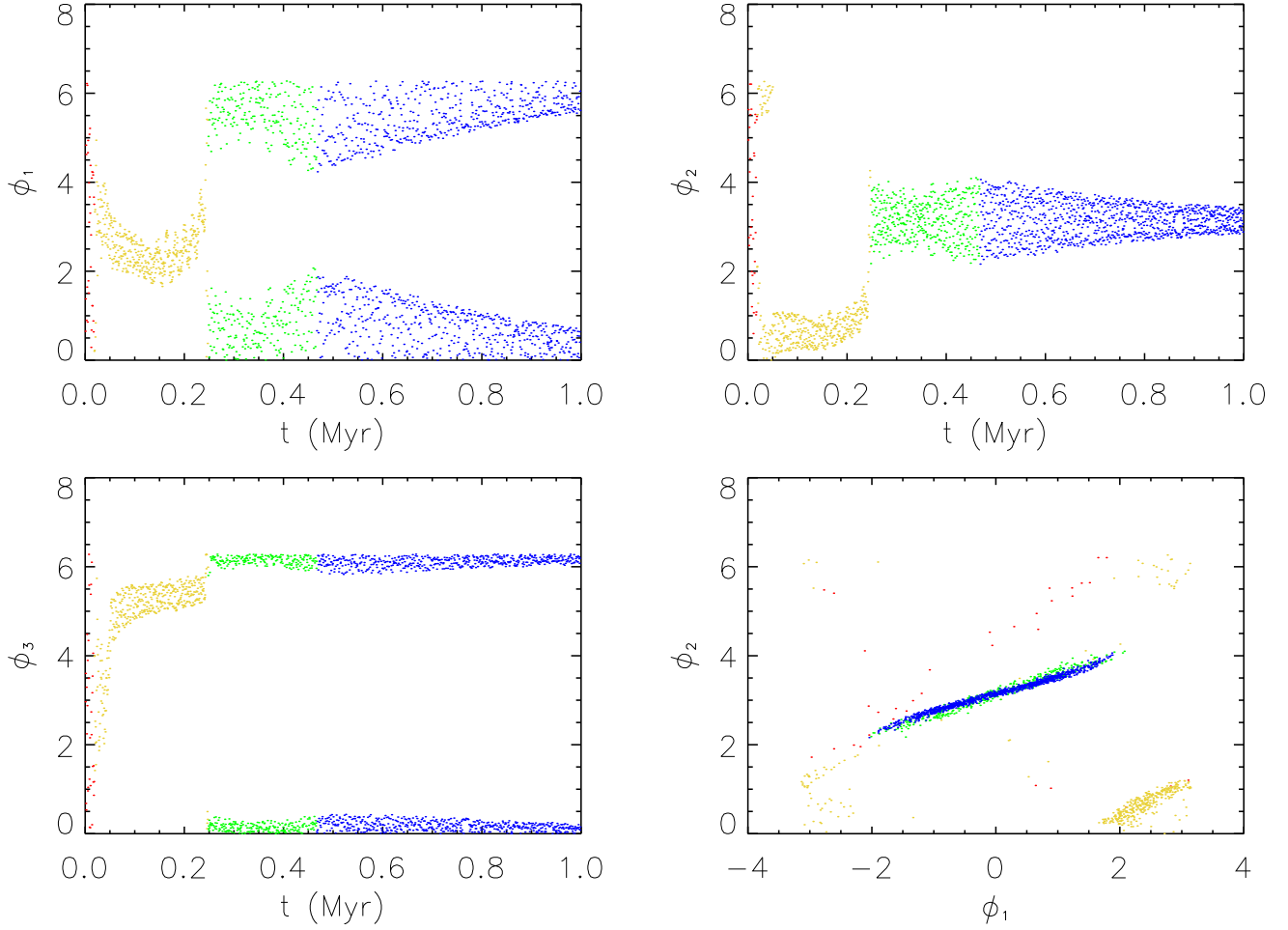


Fig. 5.— Representative behavior of the resonance angles. The first three panels show the time evolution of the 3:1 resonance angles for a representative simulation in which two equal mass planets with $m_P = 1.0 m_J$ migrate inward together and approach the 3:1 mean motion resonance. As shown here, the resonance angles exhibit complex behavior and exhibit large librations about the resonance; nonetheless, a well-defined resonant condition is reached. The lower right panel shows two of the resonance angles plotted against each other. For most of the evolution, $t > 0.25$ Myr, the system librates around the point $\phi_1 = 0$, $\phi_2 = \pi$.

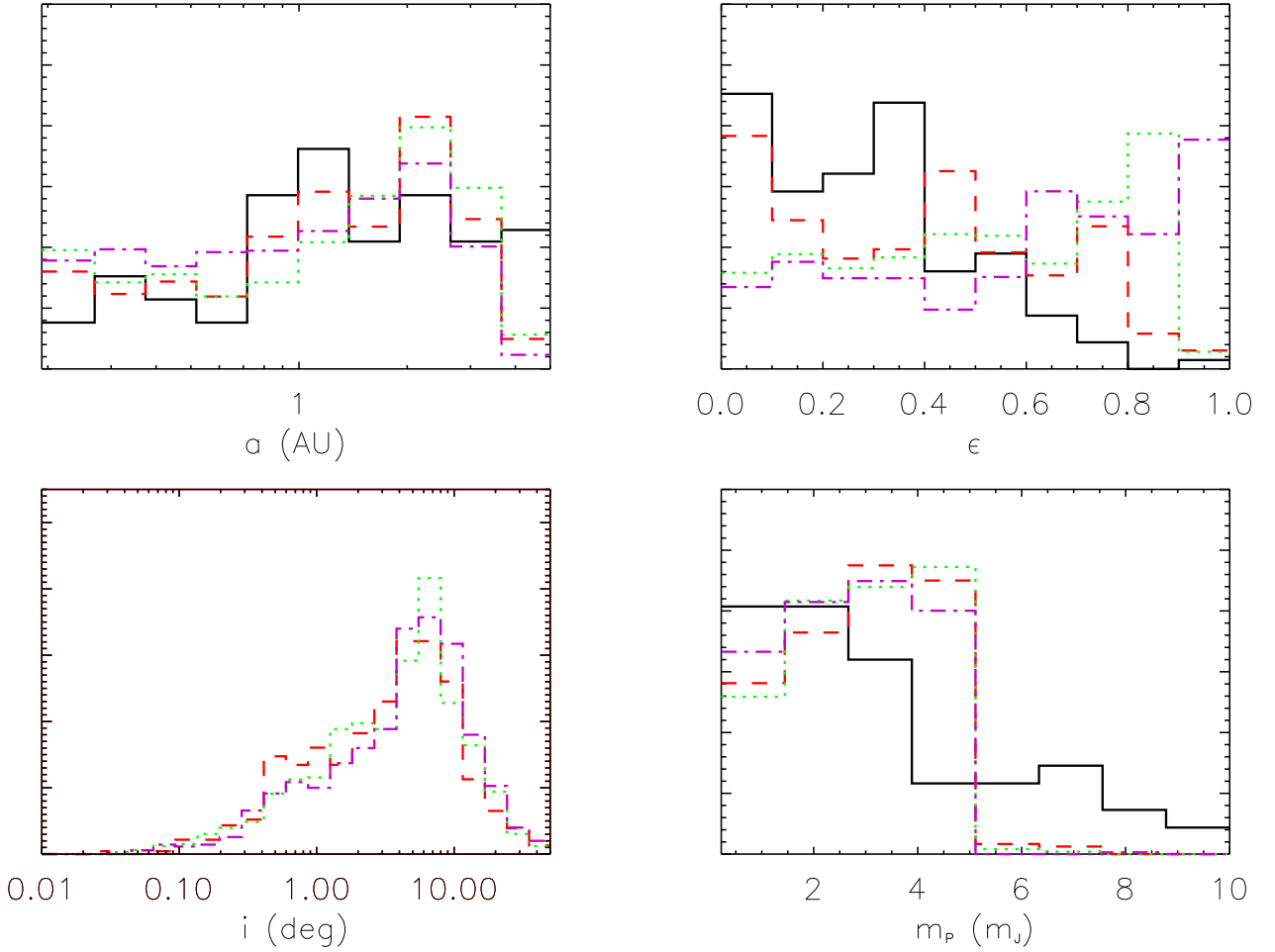


Fig. 6.— Normalized histograms of the orbital elements of surviving planets for a linear (random) planetary IMF. The upper left panel shows the distributions of semi-major axis for the observed planets (solid curve) and theoretical simulations with varying time scales for eccentricity damping: dashes ($\tau_{ed} = 0.3$ Myr), dots ($\tau_{ed} = 1$ Myr), and dot-dashes ($\tau_{ed} = 3$ Myr). Similarly, the upper right panel shows the distributions of eccentricities and the lower left panel shows the distributions of orbital inclination angles. The lower right panel shows the distributions of masses, where the mass distribution of the observed planets (solid curve) is included for comparison; note that the random IMF for the simulations cuts off at $5 m_J$.

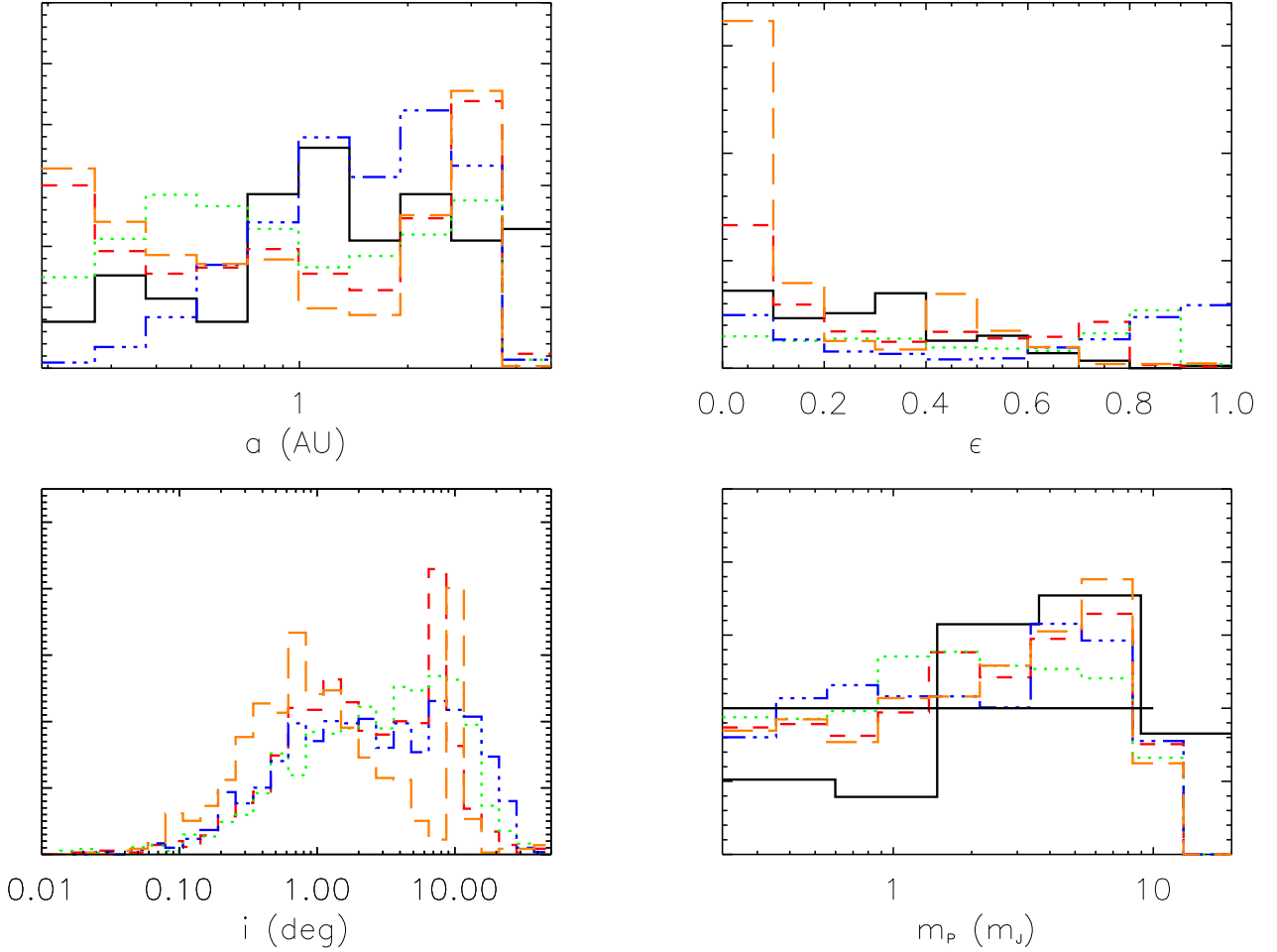


Fig. 7.— Normalized histograms of the orbital elements of surviving planets for a logarithmic (random) planetary IMF. The upper left panel shows the distributions of semi-major axis for the observed planets (solid curve) and theoretical simulations with varying time scales for eccentricity damping: long dashes ($\tau_{\text{ed}} = 0.1$ Myr), regular dashes ($\tau_{\text{ed}} = 0.3$ Myr), dots ($\tau_{\text{ed}} = 1$ Myr), and double dot-dashes ($\tau_{\text{ed}} \rightarrow \infty$). Similarly, the upper right panel shows the distributions of eccentricities and the lower left panel shows the distributions of orbital inclination angles. The lower right panel shows the distributions of masses, where the solid histogram shows the distribution of observed planets and the solid horizontal line shows starting log-random distribution; note that the log-random IMF for the simulations cuts off at $10 m_J$.

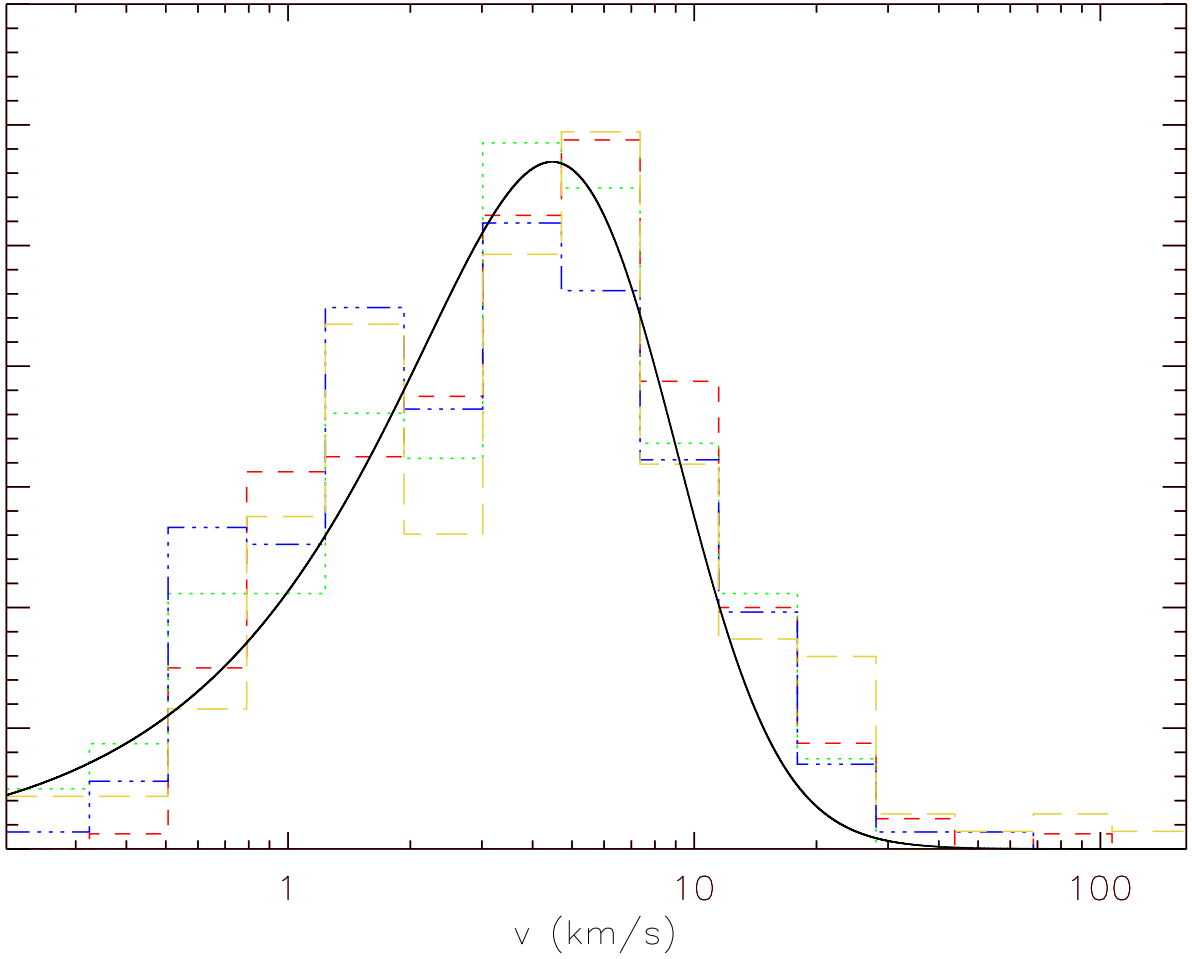


Fig. 8.— Distribution of ejection velocities for planets that are ejected during the epoch of migration. The distribution is shown for the log-random planetary IMF and for four values of the eccentricity damping time scale: $\tau_{\text{ed}} = 0.1$ Myr (yellow long-dashed curve), $\tau_{\text{ed}} = 0.3$ Myr (red short-dashed curve), $\tau_{\text{ed}} = 1.0$ Myr (green dotted curve), and $\tau_{\text{ed}} \rightarrow \infty$ (blue dot-dashed curve). The four distributions are normalized to the same value, with the vertical scale arbitrary. The smooth solid curve shows the (normalized) analytic approximation to the distribution of ejection speeds (as derived in the text). All speeds are given in km/s.

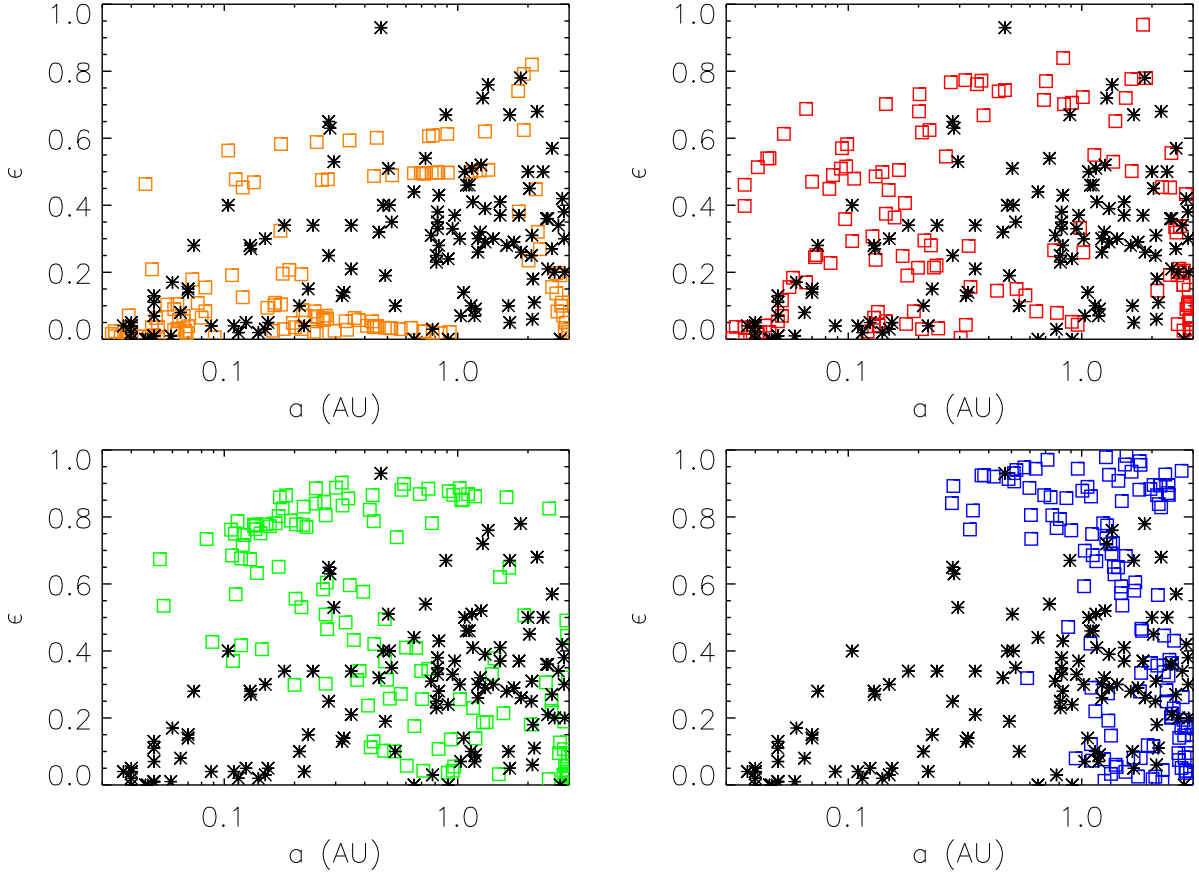


Fig. 9.— The $a - \epsilon$ plane for observed and theoretical planets, where no corrections for additional evolution have been applied to the theoretical sample. This diagram shows the semi-major axes a and eccentricities ϵ for the observed extrasolar planets as stars. The results of the theoretical simulations are shown as open squares. All of the theoretical simulations use the log-random IMF. The four panels correspond to different choices of the eccentricity damping time scale: $\tau_{\text{ed}} = 0.1$ Myr (upper left), $\tau_{\text{ed}} = 0.3$ Myr (upper right), $\tau_{\text{ed}} = 1.0$ Myr (lower left), and $\tau_{\text{ed}} \rightarrow \infty$ (lower right).

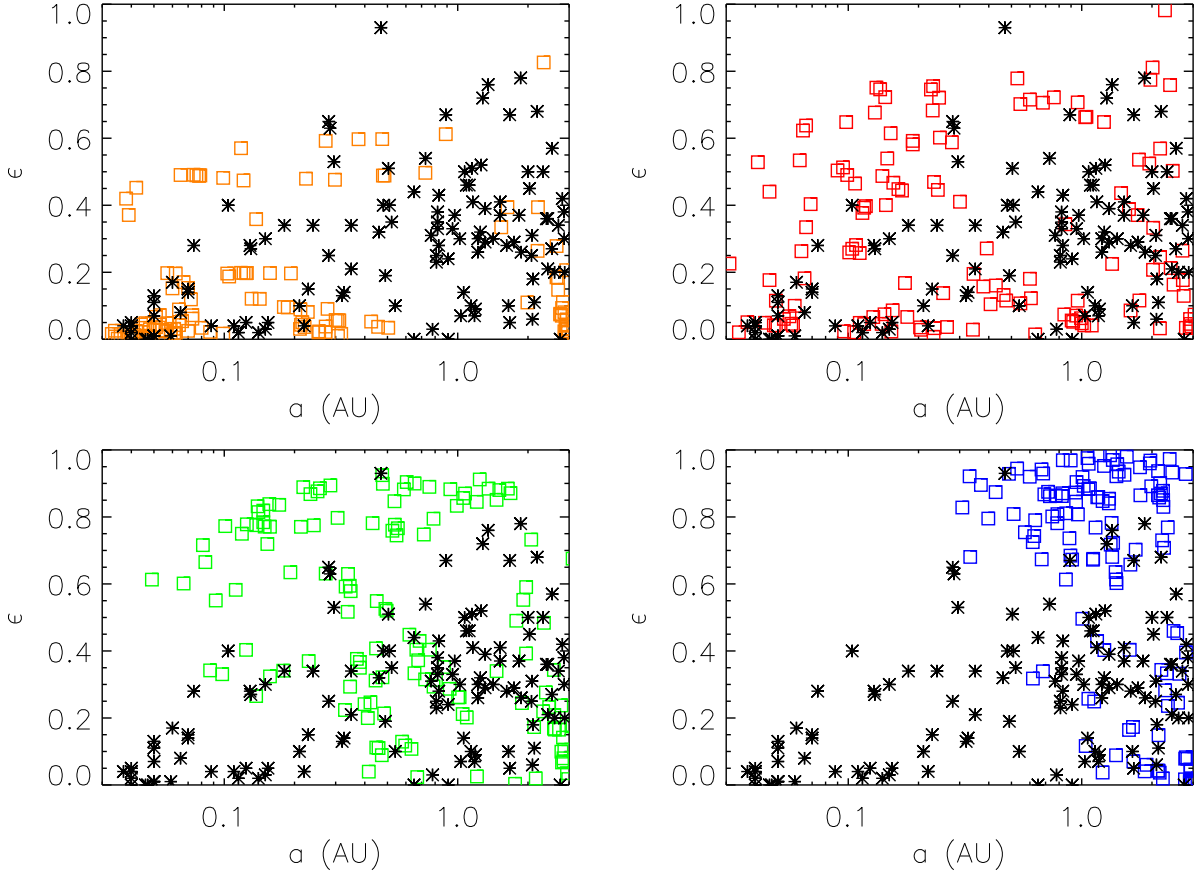


Fig. 10.— The $a - \epsilon$ plane for observed and theoretical planets, where the theoretical sample starts with a log-random IMF and has been subjected to a cut in reflex velocity k_{re} at 3 m/s. No corrections for additional evolution have been applied to the theoretical sample. This diagram shows the semi-major axes a and eccentricities ϵ for the observed extrasolar planets as stars. The results of the theoretical simulations are shown as open squares. The four panels correspond to different choices of the eccentricity damping time scale: $\tau_{\text{ed}} = 0.1$ Myr (upper left), $\tau_{\text{ed}} = 0.3$ Myr (upper right), $\tau_{\text{ed}} = 1.0$ Myr (lower left), and $\tau_{\text{ed}} \rightarrow \infty$ (lower right).

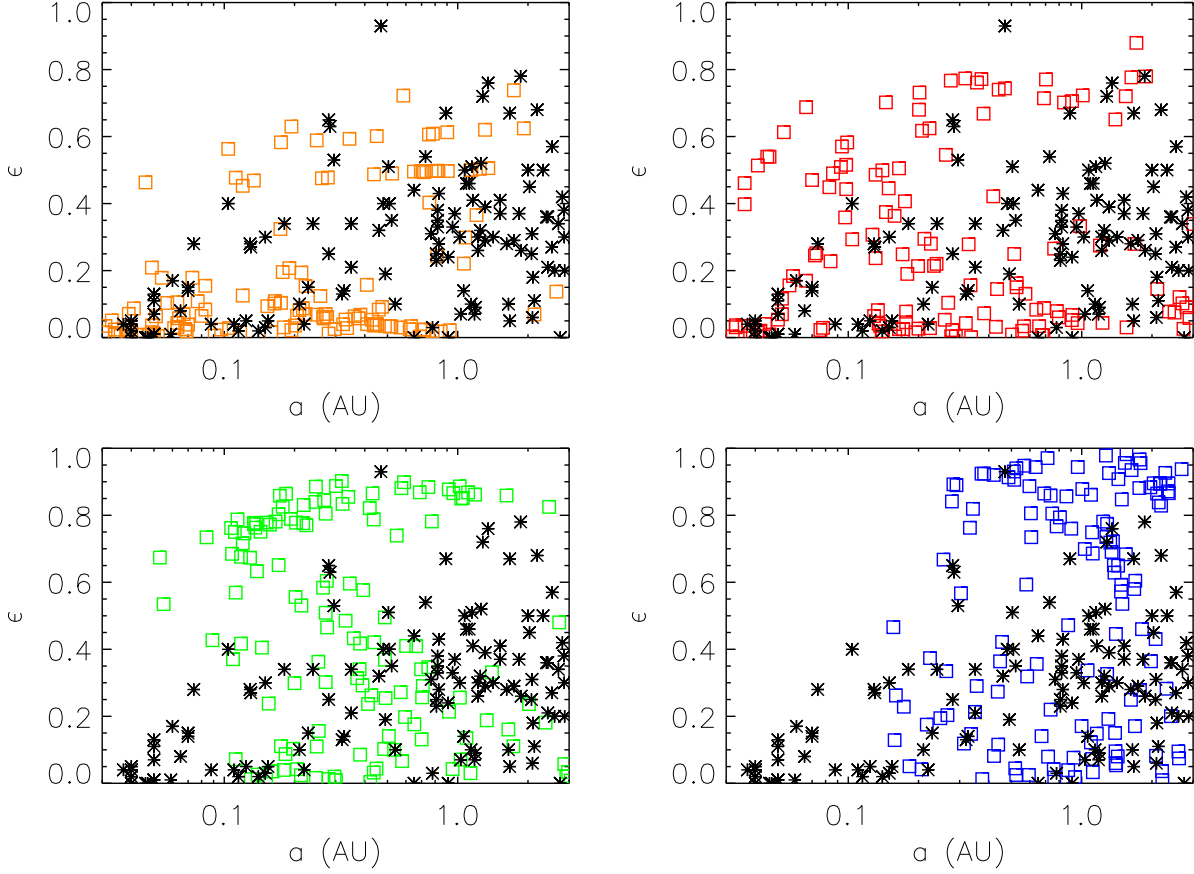


Fig. 11.— The $a - \epsilon$ plane for observed and theoretical planets, where the theoretical sample starts with a log-random IMF and has been corrected for additional orbital evolution (first algorithm). Here the disk is assumed to exist beyond the end of the numerical simulations for an additional time given by $\Delta t = \delta t - t_{sim}$, where t_{sim} is the time at the end of the simulation, δt is a random time scale in the range $0 - 1$ Myr, and negative values are set to zero. This diagram shows the semi-major axes a and eccentricities ϵ for the observed extrasolar planets as stars. The results of the theoretical simulations are shown as open squares. The four panels correspond to different choices of the eccentricity damping time scale: $\tau_{ed} = 0.1$ Myr (upper left), $\tau_{ed} = 0.3$ Myr (upper right), $\tau_{ed} = 1.0$ Myr (lower left), and $\tau_{ed} \rightarrow \infty$ (lower right).

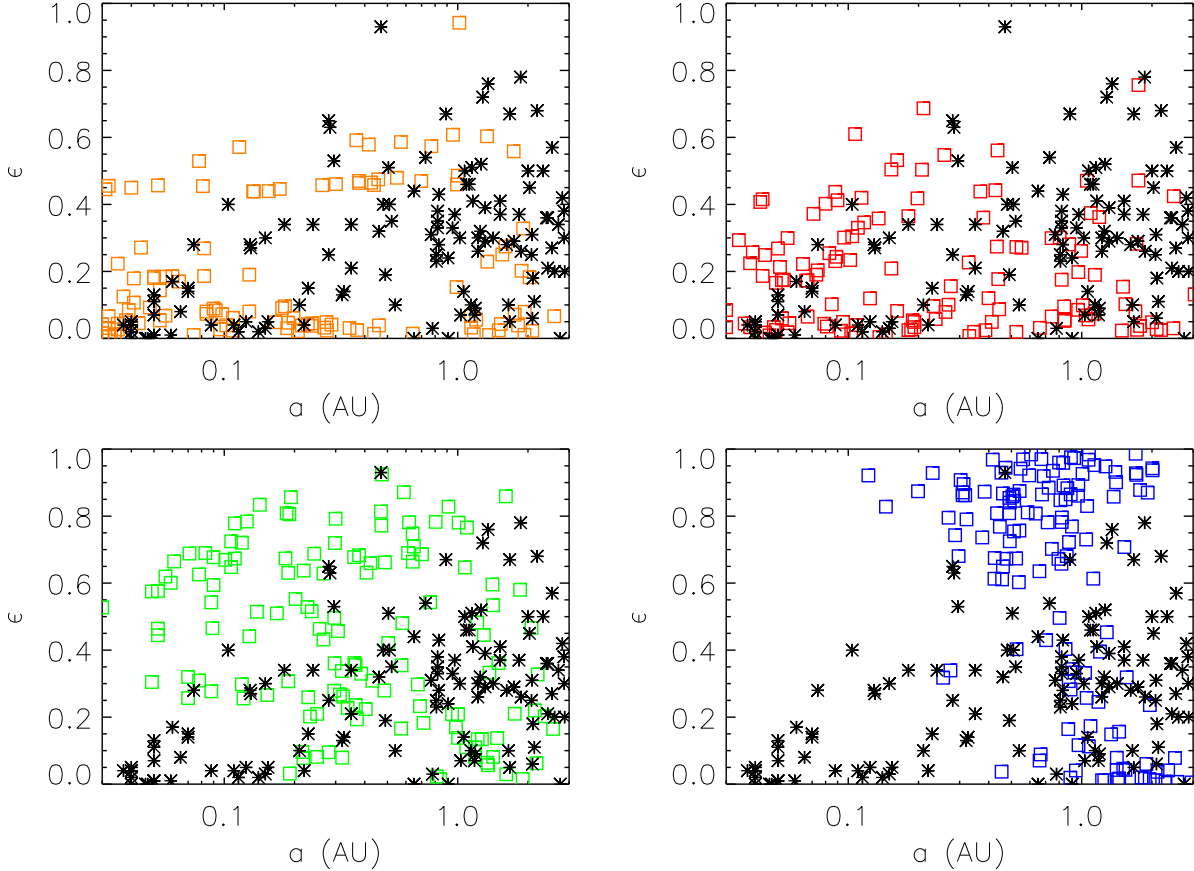


Fig. 12.— The $a - \epsilon$ plane for observed and theoretical planets, where the theoretical sample starts with a log-random IMF and has been corrected for additional orbital evolution (second algorithm). The disk is assumed to exist beyond the end of the numerical simulations for an additional time Δt , which is chosen randomly from the range 0 – 0.3 Myr. This diagram shows the semi-major axes a and eccentricities ϵ for the observed extrasolar planets as stars. The results of the theoretical simulations are shown as open squares. The four panels correspond to different choices of the eccentricity damping time scale: $\tau_{\text{ed}} = 0.1$ Myr (upper left), $\tau_{\text{ed}} = 0.3$ Myr (upper right), $\tau_{\text{ed}} = 1.0$ Myr (lower left), and $\tau_{\text{ed}} \rightarrow \infty$ (lower right).

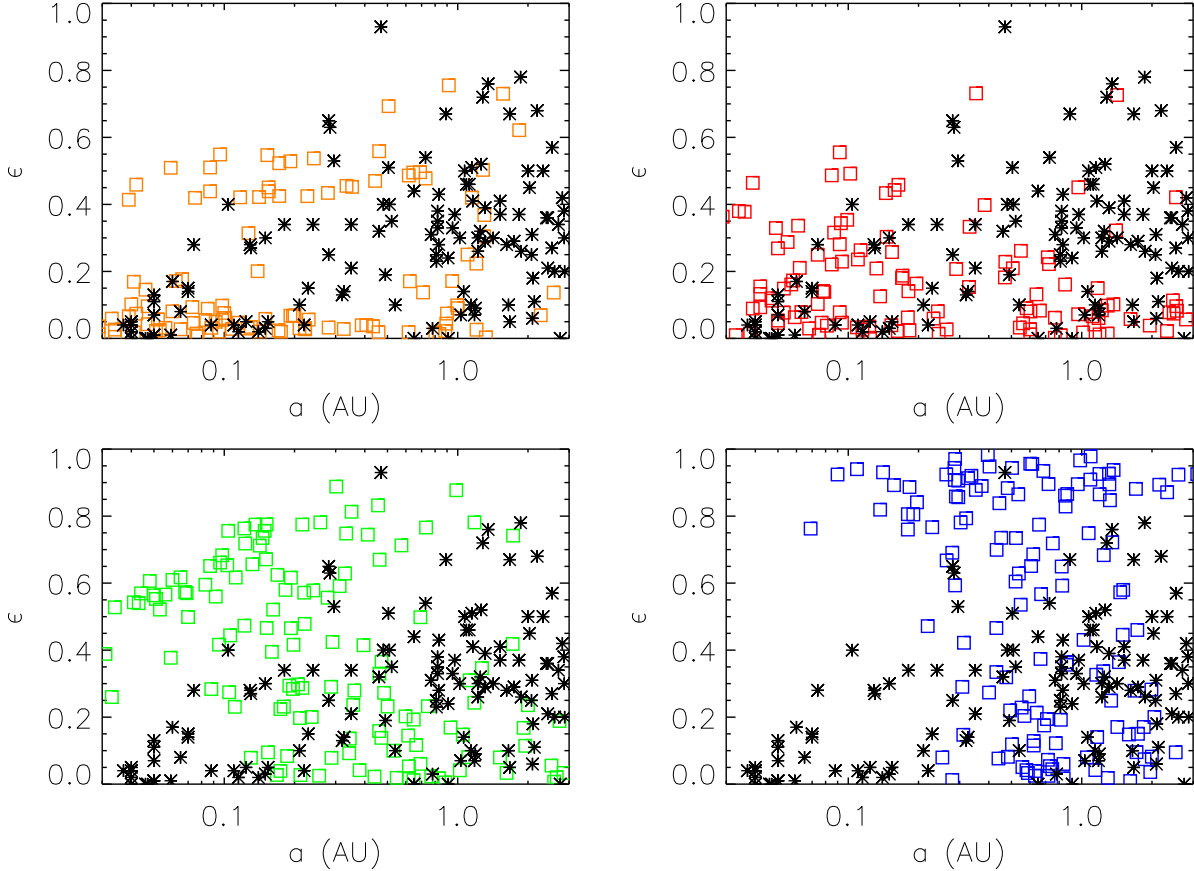


Fig. 13.— The $a - \epsilon$ plane for observed and theoretical planets, where the theoretical sample starts with a log-random IMF and has been corrected for additional orbital evolution (third algorithm). The disk is assumed to exist beyond the end of the numerical simulations for an additional time Δt , which is chosen randomly from the range 0 – 0.5 Myr. This diagram shows the semi-major axes a and eccentricities ϵ for the observed extrasolar planets as stars. The results of the theoretical simulations are shown as open squares. The four panels correspond to different choices of the eccentricity damping time scale: $\tau_{\text{ed}} = 0.1$ Myr (upper left), $\tau_{\text{ed}} = 0.3$ Myr (upper right), $\tau_{\text{ed}} = 1.0$ Myr (lower left), and $\tau_{\text{ed}} \rightarrow \infty$ (lower right).

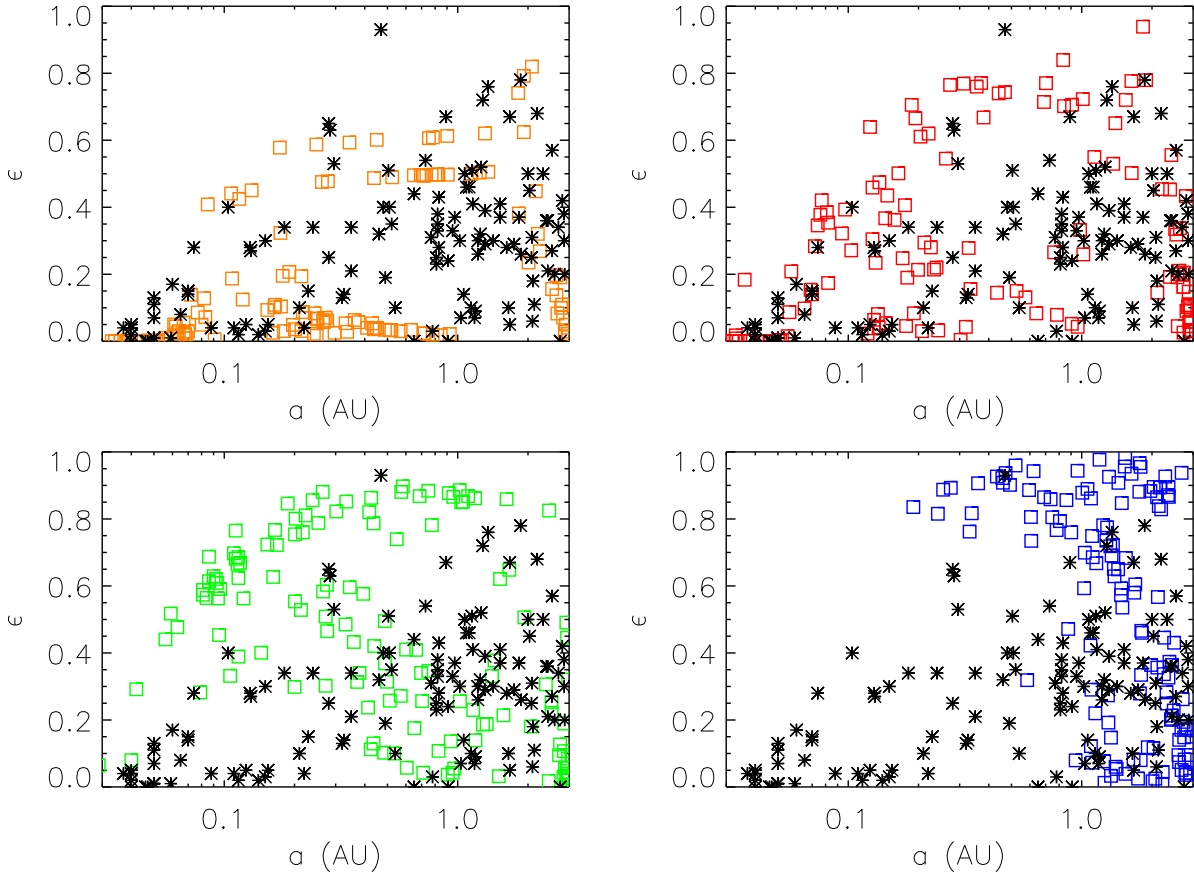


Fig. 14.— The $a - \epsilon$ plane for observed and theoretical planets, where the theoretical sample starts with a log-random IMF and has been corrected for tidal circularization over the stellar lifetime, which is assumed to lie in the range 1 – 6 Gyr. This diagram shows the semi-major axes a and eccentricities ϵ for the observed extrasolar planets as stars; results of the theoretical simulations are shown as open squares. The four panels correspond to different choices of the eccentricity damping time scale: $\tau_{\text{ed}} = 0.1$ Myr (upper left), $\tau_{\text{ed}} = 0.3$ Myr (upper right), $\tau_{\text{ed}} = 1.0$ Myr (lower left), and $\tau_{\text{ed}} \rightarrow \infty$ (lower right).

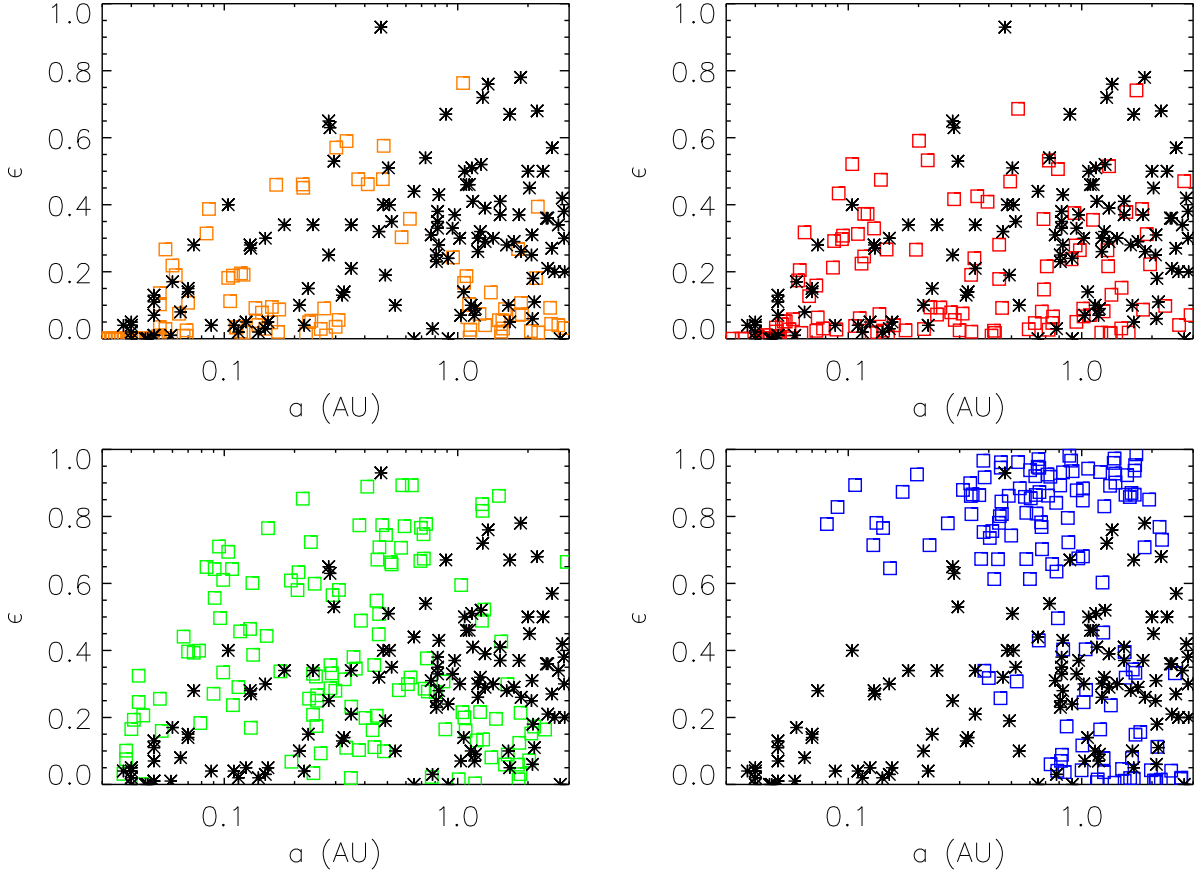


Fig. 15.— The $a - \epsilon$ plane for observed and theoretical planets using corrections for both continued disk evolution and tidal circularization. The theoretical sample starts with a log-random IMF, but a reflex velocity cut $k_{\text{re}} > 3$ m/s has been applied to the surviving planets. The disk is assumed to continue driving planet migration beyond the end of the simulations for a random time interval in the range 0 – 0.3 Myr. Tidal circularization is assumed to continue for a stellar lifetime, taken to be a random time interval in range 1 – 6 Gyr. This diagram shows the semi-major axes a and eccentricities ϵ for the observed extrasolar planets as stars; results of the theoretical simulations are shown as open squares. The four panels correspond to different choices of the eccentricity damping time scale: $\tau_{\text{ed}} = 0.1$ Myr (upper left), $\tau_{\text{ed}} = 0.3$ Myr (upper right), $\tau_{\text{ed}} = 1.0$ Myr (lower left), and $\tau_{\text{ed}} \rightarrow \infty$ (lower right).